

## RESEARCH ARTICLE

10.1002/2015JA021486

## Key Points:

- Density structures observed by MEX in the dayside Martian ionosphere above magnetic anomalies
- Structures appear as bulges with latitude extents matching with areas of near-radial  $B$  field
- Observations above the structures often indicate ionospheric plasma on closed magnetic field lines

## Correspondence to:

C. Diéval,  
c.dieval@lancaster.ac.uk

## Citation:

Diéval, C., D. J. Andrews, D. D. Morgan, D. A. Brain, and D. A. Gurnett (2015), MARSIS remote sounding of localized density structures in the dayside Martian ionosphere: A study of controlling parameters, *J. Geophys. Res. Space Physics*, 120, doi:10.1002/2015JA021486.

Received 22 MAY 2015

Accepted 23 AUG 2015

Accepted article online 27 AUG 2015

## MARSIS remote sounding of localized density structures in the dayside Martian ionosphere: A study of controlling parameters

C. Diéval<sup>1,2</sup>, D. J. Andrews<sup>3</sup>, D. D. Morgan<sup>2</sup>, D. A. Brain<sup>4</sup>, and D. A. Gurnett<sup>2</sup>

<sup>1</sup>Department of Physics, University of Lancaster, Lancaster, UK, <sup>2</sup>Department of Physics and Astronomy, University of Iowa, Iowa City, Iowa, USA, <sup>3</sup>Swedish Institute of Space Physics, Uppsala, Sweden, <sup>4</sup>Laboratory for Atmospheric and Space Physics, University of Colorado, Boulder, Colorado, USA

**Abstract** Enhanced topside electron densities in the dayside Martian ionosphere have been repetitively observed in areas of near-radial crustal magnetic fields, for periods of tens of days, indicating their long-term spatial and temporal stability despite changing solar wind conditions. We perform a statistical study of these density structures using the ionospheric mode of the Mars Advanced Radar for Subsurface and Ionosphere Sounding (MARSIS) onboard Mars Express. We estimate the apparent extents of these structures relative to the altitude of the surrounding ionosphere. The apex of the density structures often lies higher than the surrounding ionosphere (median vertical extent of 18 km), which indicates upwellings. These structures are much wider than they are high, with latitudinal scales of several degrees. The radar reflector regions are observed above both moderate and strong magnetic anomalies, and their precise locations and latitudinal extents match quite well with the locations and latitudinal extents of magnetic structures of given magnetic polarity (oblique to vertical fields), which happen to be regions where the field lines are open part of the time. The majority of the density structures occur in regions where ionospheric plasma is dominant, indicating closed field regions shielded from shocked solar wind plasma.

### 1. Introduction

In the absence of a global planetary magnetic field, the interaction of the Martian ionosphere with the solar wind generates an induced magnetosphere, which protects the atmosphere from solar wind-driven erosion. In addition, residual crustal magnetic fields have been discovered by the MGS (Mars Global Surveyor) orbiter, the strongest fields reaching  $|B|$  up to 200 nT at 400 km altitude in the southern hemisphere while smaller fields reach  $|B| < 50$  nT at 400 km in the northern hemisphere [e.g., *Acuña et al.*, 1999].

The subject of the present paper is topside daytime electron density structures found in areas of usually near-radial crustal fields, previously investigated by *Gurnett et al.* [2005], *Duru et al.* [2006], *Nielsen et al.* [2007a], and *Andrews et al.* [2014]. Here we present the results of a statistical study of these structures with a combination of remote ionospheric soundings by MARSIS (Mars Advanced Radar for Subsurface and Ionosphere Sounding) and of in situ electron energy distribution measurements by ASPERA-3 (Analyzer of Space Plasmas and Energetic Atoms) onboard the MEX (Mars Express) orbiter.

MEX, in orbit around Mars since late December 2003, follows a near-polar orbit of period  $\sim 7$  h, with pericenter  $\sim 300$  km and apocenter  $\sim 10,000$  km. Its payload notably includes two instruments which we will use here: MARSIS (Mars Advanced Radar for Subsurface and Ionosphere Sounding) and ASPERA-3 (Analyzer of Space Plasmas and Energetic Atoms), which are respectively described by *Picardi et al.* [2004] and *Barabash et al.* [2006].

On the dayside, remote soundings of the topside ionosphere by MARSIS permitted the discovery of localized density structures in areas of usually near-radial crustal fields [*Gurnett et al.*, 2005]. The apparent altitude of the density structures detected by MARSIS is often higher than the apparent altitude of the surrounding "main" ionosphere at the same density level, with a mean vertical extent of  $\sim 20$  km, suggesting an ionospheric upwelling [*Gurnett et al.*, 2005; *Duru et al.*, 2006]. The strongest magnetic anomalies in the southern hemisphere tend to be elongated over several tens of degrees in longitude, and the multiple detection of the density structures over consecutive MEX passes above the same magnetic anomaly suggests that the density structures are also elongated in longitude, probably shaped like half-cylinders [*Gurnett et al.*, 2005; *Duru et al.*, 2006].

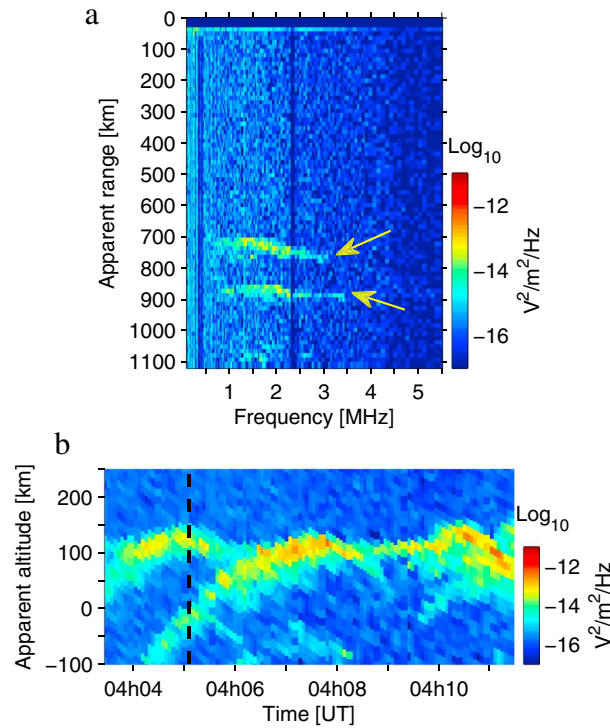


**Figure 1.** (a) Example of a MARSIS ionogram (orbit 4198, 13 April 2007, 04:05:06 UT). The intensity of the received echo (color coded) is shown as a function of the sounding frequency (horizontal axis) and of the apparent range (vertical axis). (b) Example of a MARSIS echogram (orbit 4198). The vertical axis is the apparent altitude of the received echo. The color coding is the intensity of the received echo averaged over the frequency range 1.8–2 MHz. The black vertical dashed line indicates the time corresponding to the ionogram in Figure 1a.

of the electron temperature due to heating of the atmosphere by precipitating electrons may indirectly increase the electron density through a reduction of the ion-electron recombination rate. *Andrews et al.* [2014] also suggested mechanisms which involved Joule heating of the atmosphere by field-aligned currents and Pedersen currents [*Withers et al.*, 2005; *Fillingim et al.*, 2010, 2012; *Riousset et al.*, 2013, 2014]. Finally, *Matta et al.* [2015] proposed that these density structures arise from field-aligned transport along near-radial field lines, without involving heating. We propose in this paper to use a statistical study of MARSIS data to identify some of the controlling factors of the dayside density structures, in order to better constrain their formation process. By doing this, we may be able to reduce the number of alternative explanations. In particular, with the help of in situ plasma measurements by ASPERA-3, we may check the hypothesis of the role of solar wind electron precipitation. In section 2, we will describe the instruments and method. In section 3, we will describe the results. In section 4, we will present a discussion of results and section 5 will be the summary and conclusion.

## 2. Instruments and Method

MARSIS operates in the active ionospheric sounding mode and the subsurface mode [*Picardi et al.*, 2004]. We use here the active ionospheric sounding mode, in which a 40 m tip-to-tip dipole antenna, mounted normally to the direction of spacecraft motion, transmits sinusoidal pulses of duration 91.4  $\mu$ s over a frequency sweep of 160 steps from 0.1 to 5.4 MHz (frequency resolution  $\Delta f/f \approx 2\%$ ). At each sounding frequency, the signal propagates until it becomes reflected by a layer with the same plasma frequency as the transmitted frequency. The receiver measures the time delay  $t_{\text{delay}}$  for receiving this echo in 80 time bins ranging from 259.3  $\mu$ s to 7.86 ms after the start of the pulse. During this process, the radar can remotely sample layers of increasing plasma density at decreasing altitudes, down to the ionospheric peak. The resulting matrix of

Furthermore, *Nielsen et al.* [2007a] have found strong horizontal density gradients across the density structures observed by MARSIS, with isodensity contours which can be very inclined with respect to the horizontally stratified surrounding main ionosphere, sometimes even vertical slabs. This suggests an easier vertical diffusion of the plasma along the near-radial fields. Finally, *Andrews et al.* [2014] reported that these density structures tend to be stable for several consecutive passes of MEX in a given geographic area (over intervals of tens of days), suggesting that they easily reform, despite the rapidly changing magnetic configuration at ionospheric altitudes and the varying upstream solar wind conditions. This magnetic configuration evolves due to the varying IMF (interplanetary magnetic field) and the varying position of the crustal fields with respect to the Sun caused by Mars' rotation.

Several explanations have been proposed for the formation process of the dayside density structures. *Gurnett et al.* [2005] suggested that the precipitation of solar wind electrons into a magnetic cusp region may heat the atmosphere until it inflates and diffuses upward, increasing the scale height and therefore displacing a given isodensity contour to higher altitude. *Andrews et al.* [2014] alternatively proposed that an increase

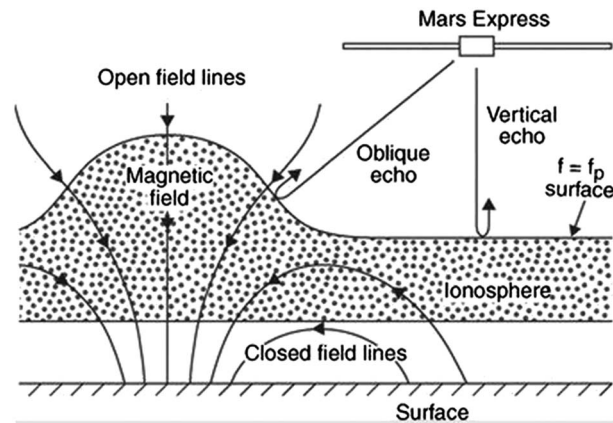


**Figure 2.** Sketch adapted from Gurnett *et al.* [2005], illustrating a possible mechanism for generating the oblique ionospheric echoes detected by MARSIS. The sketch represents an idealized situation where MARSIS measures both a vertical echo from the horizontally stratified ionosphere and an oblique echo from a distant density structure located in an area of near-radial crustal fields. From Gurnett *et al.* [2005]. Reprinted with permission from the American Association for the Advancement of Science.

received intensity as a function of time delay and sounding frequency is obtained in 1.26 s and is called an “ionogram.” The full frequency sweep is repeated every 7.54 s.

An example of MARSIS data from orbit 4198 is shown in Figure 1. More examples will be shown later in Figures 9 and 10. Figure 1a shows an ionogram. The time delay was transformed to the apparent range, which is the distance traveled by the pulse by assuming no dispersion, calculated as  $c \cdot t_{\text{delay}}/2$ , where  $c$  is the speed of light in the vacuum. Two ionospheric traces are visible, marked by arrows. The echo with the shorter range (between 700 and 800 km) corresponds to the near-vertical reflection from the ionosphere below MEX; we will see later that the spacecraft was actually passing directly above the apex region of a density structure. The echo with the longer range

(between 800 and 900 km) corresponds to an oblique reflection from another distant density structure, with isodensity contours being inclined with respect to the horizontal.

These oblique echoes are detected for several consecutive ionograms. An echogram at a fixed sounding frequency consists of ionograms cut at this frequency and stacked together in a time series. Figure 1b shows an example of echogram for orbit 4198, averaged over 1.8–2 MHz. The altitude of MEX was subtracted from the apparent range to obtain the apparent altitude. We note that the apparent altitude is lower than the real altitude, since the dispersion, uncorrected here, causes the signal to propagate more slowly as it approaches the point where it gets reflected, and thus, the signal seems to have an apparent reflection further from the spacecraft. The near-vertical reflection from the almost horizontally stratified “main ionosphere” appears as a near horizontal line near 100–120 km apparent altitude (for example, at 04:09:00–04:09:30 UT). We also see numerous downward-facing hyperbola traces, which are the signatures of the localized density structures we are interested in. The apexes of these hyperbola traces are often higher than the surrounding ionosphere trace [Gurnett *et al.*, 2005; Duru *et al.*, 2006]; this is the case in Figure 1b for the hyperbolas with the apexes of apparent altitude 153 km at 04:05:00 UT, 145 km at 04:07:30 UT, and 158 km at 04:10:30 UT. The time of the ionogram from Figure 1a is indicated by the black vertical dashed line. This vertical line intersects two ionospheric traces of different apparent altitudes, one at ~150 km and one at ~0 km, corresponding respectively to the near-vertical reflection and to the oblique reflection in Figure 1a. When the spacecraft is located away but still within reflection range from a density structure, MARSIS ideally detects both the vertical echo from the horizontally stratified ionosphere below and the oblique echo from the distant density structure. This situation is illustrated in the sketch of Figure 2, adapted from Gurnett *et al.* [2005]. Motion toward (away) from the distant reflection region shows up as increasing (decreasing) apparent altitude of the oblique echoes, explaining the hyperbola shape in the echogram. MARSIS measures the near-vertical echo from the density structure when the spacecraft passes overhead; this corresponds to the situation where the apex of the hyperbola lies at or above the surrounding “main” ionosphere trace in the echogram.

We use the list of 1126 dayside oblique echoes established from the previous work by Andrews *et al.* [2014]. These authors considered sequences of at least five orbits of MEX with at least 200 MARSIS ionograms each, with consecutive passes above specific geographic areas and where gaps of two consecutive orbits maximum were allowed. Andrews *et al.* [2014] selected data when the spacecraft was at altitudes  $<1100$  km and at solar zenith angles  $<90^\circ$ . The altitude restriction corresponds to the maximum range at which the radar can remotely detect an ionospheric layer. These authors examined the MARSIS echograms of these orbits to identify hyperbola traces and selected the most obvious cases (oblique echoes well separated from the “main” surrounding ionosphere trace for at least five successive ionograms) for

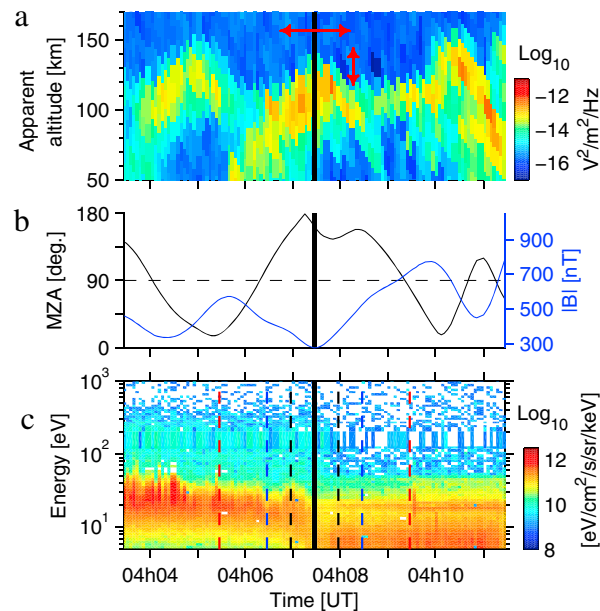


**Figure 3.** Time series during orbit 4198. The time span is the same as in Figure 1b. The black vertical solid line in all panels marks the time of the hyperbola apex. (a) MARSIS echogram averaged over 1.8–2 MHz. The vertical red arrow indicates the vertical extent of the hyperbola apex at or above the surrounding ionosphere trace. The horizontal red arrow marks the time interval during which the hyperbola stays at or above the surrounding ionosphere trace. (b) Crustal magnetic field model [Cain *et al.*, 2003] evaluated at 150 km altitude at the footprint of MEX. Left axis: magnetic zenith angle MZA (black). The black horizontal dashed line marks MZA = 90°, i.e., horizontal field. Right axis: magnetic field strength (blue). (c) ELS electron energy time spectrogram. The vertical axis is the electron energy, and the color coding is the omnidirectional differential energy flux averaged over sectors 2 to 11. The white color means flux at the background level. The vertical dashed lines indicate time intervals around the hyperbola apex time, for which we will examine the plasma conditions: ±30 s (black), ±1 min (blue), and ±2 min (red).

situ 2-D energy distributions of electrons formerly collimated into the plane of the instrument aperture, in the energy range 5 eV to 20 keV (energy resolution  $\Delta E/E = 8\%$ ) with a 4 s time resolution. At low altitudes above Mars, the measurement plane of ELS is oriented such that it is able to detect particles moving upward, downward, and parallel to the planetary surface. We note that the detection of particles moving downward (including electron precipitation) is affected by the shadowing of certain ELS sectors by the body of MEX [e.g., Soobiah *et al.*, 2013]. In consequence, we will not use the downward differential fluxes, but rather the omnidirectional differential fluxes for sectors 2–11, which were not blocked by the spacecraft.

### 3. Results

#### 3.1. Basic Characteristics of the Density Structures

In this section, we will determine the apparent extents of the hyperbola traces from the echograms taken at a fixed frequency of 1.9 MHz (corresponding density  $4.47 \cdot 10^4 \text{ cm}^{-3}$ ), a typical frequency at which the oblique echoes are observed. Figure 3a shows a zoom-in of the echogram from Figure 1b. The vertical red arrow represents the vertical extent of the apex compared to the level of the surrounding “main” ionosphere trace, using the approach of Duru *et al.* [2006]. The horizontal red arrow represents the time interval during which the hyperbola stays at or above the surrounding ionosphere trace. From this time interval, we calculate the corresponding extent along MEX track, by using the spacecraft velocity (~4 km/s at pericenter, much faster

performing a quadratic polynomial fitting. Then Andrews *et al.* [2014] discarded the oblique echoes which were ill-fitted. For this reason, the list is not exhaustive. However, this is not an issue because we do not attempt to determine the occurrence frequency of observing oblique echoes during all the orbits considered by Andrews *et al.* [2014], but we are rather interested in the statistical properties of several aspects relative to the oblique echoes. This procedure left 1126 hyperbola traces, which were detected on 437 orbits, spanning August 2005 to February 2013, which we will use here.

Three aspects relative to the oblique echoes are illustrated in three panels in Figure 3 for a time series on orbit 4198, for the same time interval as in Figure 1b. The description of Figure 3 will be done for convenience in section 3 with one panel per subsection. Section 3.1 treats some basic characteristics of the reflection regions, which we will determine from the echograms. Then, section 3.2 treats the relationship between the magnetic anomalies and the reflection regions. Finally, section 3.3 treats the plasma conditions detected at the times that the spacecraft flies over the density structures, by using the in situ electron distribution measurements by the ELS (electron spectrometer), part of ASPERA-3.

ASPERA-3 includes two energetic neutral atom detectors and two ion and electron detectors [Barabash *et al.*, 2006]. We use ELS in the instrumental mode during which the top-hat electrostatic analyzer measures in

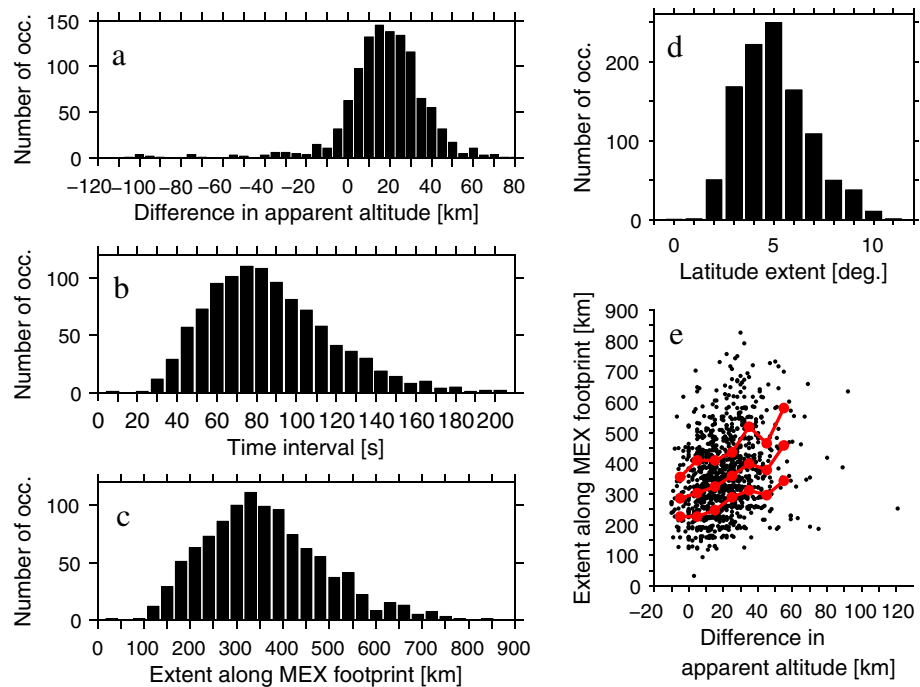


**Figure 4.** (a–d) Histograms of spatial and temporal extents of the hyperbola apex at or above the surrounding ionosphere trace, from the echogram at frequency = 1.9 MHz. (a) Vertical extent in apparent altitude. (b) Time intervals during which the hyperbolas stay at or above the surrounding ionosphere. (c) Corresponding extent along MEX footprint, using MEX velocity. (d) Corresponding latitudinal extent. (e) Scatterplot of the vertical extent versus the extent along MEX footprint. The 25th, 50th, and 75th percentiles of the extent along MEX footprint are indicated by red curves (in ascending order from the bottom of the plot), and calculated in intervals of 10 km.

than the planetary rotation) and by assuming that the density structure is time independent and immobile with respect to the surface of the planet. We note that the ionograms have a time resolution of 7.54 s and a range resolution of  $\sim 14$  km, which cause an uncertainty in the determination of the apparent extent (both vertical and along the spacecraft track) and time interval. We remark that the ionospheric traces are typically “thick,” covering several bins of apparent range (see Figure 1), so we always use the top of the bin with the shortest range (highest apparent altitude), which should correspond to a vertical reflection. In addition, the trace of the surrounding “main” ionosphere is sometimes seen to be “wavy” in the echogram, probably indicative of large altitude fluctuations of this particular isodensity contour at  $4.47 \cdot 10^4 \text{ cm}^{-3}$  [e.g., Gurnett *et al.*, 2010]. In this case, we simply take the average apparent altitude of the surrounding ionosphere trace. Finally, the extents determined from the echogram are apparent extents, not real extents, since the echogram is uncorrected for the signal dispersion due to its propagation through the plasma. The apparent extents are straightforward to determine, unlike the real extents which require a correction procedure not applicable to all the density profiles for reasons explained by, e.g., Morgan *et al.* [2008]. However, we assume for now that the qualitative statistical trends for the uncorrected extents will be the same as for the corrected ones. The study of the real shape of the density structures may be determined by using these corrected profiles of density versus real altitude. The determination of the real extents and shapes will help to better constrain the nature and the causes of these structures and is left to future work, in which we will take into account the full range of densities covered by this statistical data set of density structures and the altitudes at which they occur.

At first, we use the 1126 oblique echoes obtained from the procedure applied by Andrews *et al.* [2014]. Figure 4a shows the histogram of the vertical extents  $\Delta h$  of the hyperbola apexes relative to the surrounding “main” ionosphere trace. In agreement with the results from Gurnett *et al.* [2005] and Duru *et al.* [2006], the difference of apparent altitude between the apexes and the surrounding ionosphere is positive for the majority of the cases, suggesting ionospheric upwellings, with 25th, 50th, and 75th percentiles of 8 km, 18 km, and 29 km, respectively. The negative  $\Delta h$  values correspond to situations where the spacecraft detects

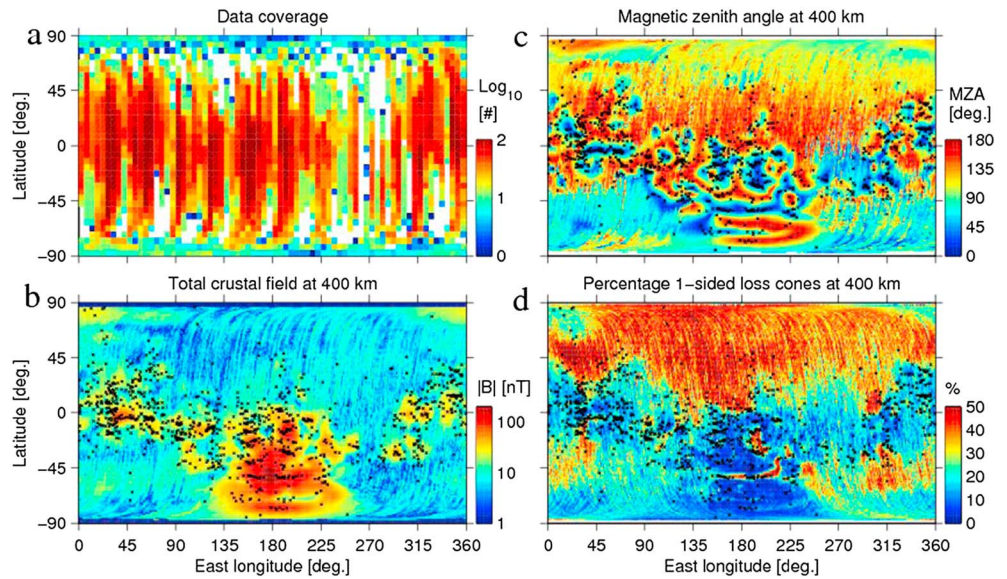
a distant density structure and does not pass overhead. The smallest value is  $-184$  km, and the largest value is  $121$  km (not shown in the range of the histogram). The large values of  $\Delta h$  are probably overestimated due to significant signal dispersion, which is not corrected in the present work. In the rest of the paper, we want to study the density structures for which MEX flies overhead, i.e., the hyperbolas whose apexes stay at or above the surrounding ionosphere trace,  $\Delta h \geq 0$  km. We consider the margin of error due to the range resolution of  $14$  km and to the occasionally disturbed surrounding ionosphere, so we also include hyperbolas with small absolute values of negative  $\Delta h$ , such as  $\Delta h > -10$  km. For the rest of the paper, we thus keep 1066 cases whose apexes are at the same level or above the surrounding ionosphere trace. Note that the majority of these cases (977 cases) have  $\Delta h > 0$ , which is interpreted as an ionospheric upwelling [e.g., Gurnett *et al.*, 2005; Duru *et al.*, 2006].

Figure 4b shows the histogram of the time intervals during which the hyperbola apexes lie at or above the surrounding ionosphere trace. The distribution has 25th, 50th, and 75th percentiles of  $61$  s,  $83$  s, and  $106$  s, respectively, and a tail toward high values. The shortest interval is  $8$  s (spanning one ionogram), and the longest interval is  $204$  s (spanning 27 ionograms). The time it takes for MEX to fly over a density structure typically corresponds to several ionograms (median number of ionograms: 11), with one ionogram produced every  $7.54$  s. This means that the density structures are stable over these time intervals. In fact, the radar usually detects these structures already for a certain time before passing overhead and still a certain time after that (the ascending and descending branches of the hyperbola traces, which can cover from one to a few tens of ionograms each). So the actual time for which these structures remain stable is even longer than the intervals shown in Figure 4b, at least as long as the time for which the radar is within reflection range from the structure, and probably much longer (hours?).

Figure 4c shows the histogram of the extents along the direction of the MEX track for which the hyperbola trace lies at or above the surrounding ionosphere trace. These extents are calculated using the corresponding time interval (from Figure 4b) and the spacecraft velocity (dependent on altitude), and the fact that the radar flies much more rapidly over the density structure than the planet rotates. The distribution has 25th, 50th, and 75th percentiles of  $263$  km,  $347$  km, and  $437$  km, respectively, and a tail toward high values. The shortest distance is  $32$  km, and the longest distance is  $827$  km. The apparent extents of the hyperbola traces at or above the surrounding ionosphere trace are typically several hundreds of kilometers, and we expect that the real extents of the density structures will be of the same order of magnitude. So the density structures are not "points" but are rather wide regions where the isodensity contours are elevated compared to the surrounding horizontally stratified ionosphere.

At latitudes away from the poles, the footprint of the spacecraft moves primarily in latitude and a little in longitude, due to its near-polar orbit. Figure 4d shows the histogram of the latitude extents during which the hyperbola trace lies at or above the surrounding ionosphere trace. These latitude extents can be determined from the latitude range spanned by MEX during the time intervals (from Figure 4b). The latitude extent is a good approximation for the angular extent along the spacecraft track, for the majority of the density structures, which are located away from the poles as we will see later. The distribution has 25th, 50th, and 75th percentiles of  $3.7^\circ$ ,  $4.9^\circ$ , and  $6.2^\circ$ , respectively, and a tail toward high values. The shortest latitude extent is  $0.5^\circ$ , and the largest latitude extent is  $10.9^\circ$ . So the apparent latitude extents are typically several degrees wide in latitude, and we expect the real latitude extents to be of the same order of magnitude.

Figure 4e shows the scatterplot of the vertical extents of the hyperbola traces with respect to the surrounding ionosphere trace versus the extents along MEX footprint (using Figures 4a and 4c). The median and quartiles of the extents along MEX footprint are represented by the red curves and calculated in steps of  $10$  km. The extents along the spacecraft track are one order of magnitude larger than the vertical extents, meaning that the density structures are much wider than they are high. Despite a large scatter of points, there is a weak positive linear relationship between the extent along the spacecraft footprint and the vertical extent, with a Pearson linear correlation coefficient of  $0.27$ . The  $p$  value for testing the hypothesis of no correlation against the alternative that there is a nonzero correlation gives  $1.13 \cdot 10^{-18}$ , which is significant at the 5% level. The increases of the median and quartile curves confirm this trend. Therefore, for a given isodensity contour, it seems that the higher the density structure appears above the surrounding ionosphere, the wider this structure becomes. Another way to interpret this finding is to consider that a density structure which is more highly elevated above the background ionosphere is probably visible over a larger range of distances along the spacecraft track.



**Figure 5.** (a) Map of the MARSIS data coverage. The color coding indicates the number of ionograms. (b and c) Map of the magnetic field strength and map of the magnetic zenith angle for the crustal fields measured at  $\sim 400$  km altitude by MGS, from *Connerney et al.* [2001]. (d) Map of the percentage of one-sided loss cone pitch angle distributions for  $\sim 115$  eV electrons measured at  $\sim 400$  km altitude on the dayside of Mars by MGS, from *Brain et al.* [2007]. In all panels, the black dots mark the locations of the hyperbola apexes.

### 3.2. Influence by the Magnetic Anomalies

We return to Figure 3 for an illustrative case study of orbit 4198. Figure 3b shows the crustal magnetic field model of *Cain et al.* [2003], evaluated at 150 km altitude at the footprint of MEX. The choice of 150 km altitude was made for consistency with previous works on this topic [e.g., *Gurnett et al.*, 2005]. The blue curve (right axis) shows the field strength  $|B|$ , and the black curve (left axis) shows the MZA (magnetic zenith angle), i.e., the angle of the magnetic field vector with respect to the zenith;  $0^\circ$  is vertical upward. The actual magnetic field configuration may change due to the superposition of the crustal fields and of the varying induced ionospheric field; nevertheless, moderate and strong crustal fields should dominate the field contribution at 150 km altitude during most of the time. During the interval shown in Figure 3, MEX flew above regions of large field strength  $> 300$  nT. The three hyperbolas previously noted in the echogram tend to coincide with near-radial fields, i.e., with the apex at MZA =  $26^\circ$  at 04:05:00 UT,  $163^\circ$  at 04:07:30 UT, and  $32^\circ$  at 04:10:30 UT. Previous studies have focused on the orientation of the crustal field [e.g., *Andrews et al.*, 2014, and references therein], which is undoubtedly an important controlling factor for the density structures. We will use the larger data set provided by *Andrews et al.* [2014] to investigate some crustal field parameters evaluated at the footprint of MEX. We will use the calculated strength and angle of the field vector with respect to the vertical for the magnetic field at 150 km altitude from the model of *Cain et al.* [2003].

We also would like to determine whether the crustal field lines were open or closed at the times of the observations of the density structures. For this, we would need observations of electron pitch angle distributions at the position of MEX when it passes above the reflection regions, which was not possible due to the lack of a magnetometer. However, the long-term stability of the density structures [*Andrews et al.*, 2014] suggests that this is not critical. Instead, we use the map of percentage of  $\sim 115$  eV electron one-sided loss cone pitch angle distributions (distributions with one loss cone) observed at  $\sim 400$  km altitude on the dayside of Mars by MAG/ER onboard MGS [*Brain et al.*, 2007, Figure 11b]. This is a statistical result averaged over several years. One-sided loss cone distributions mean that the return flux of 115 eV electrons moving along the field lines is reduced compared to the incident flux. These incident electrons can be lost in the collisional atmosphere (below the exobase at 180 km altitude), when the IMF intersects the exobase in the weakly magnetized northern hemisphere and when open field lines connect the Martian crust to the IMF in areas of near-radial fields. Incident 100 eV electrons may penetrate down to 160 km altitude in the Martian atmosphere [e.g., *Detrick et al.*, 1997], where they deposit most of their energy.

Before examining the spatial occurrence of the oblique echoes, we first show in Figure 5a the map of the data coverage of MARSIS for the orbits of MEX which, first, followed the criteria imposed in section 2 and, second, for which were detected the 1066 oblique echoes used in the rest of the study. The data coverage contains 80,966 ionograms. By comparison, there are 12,343 ionograms comprised by the time intervals during which the 1066 hyperbola apexes lie at or above the surrounding ionosphere trace. The coverage is best at altitudes away from the poles and is relatively uniform across the range of longitudes, at least near the equator. In all panels of Figure 5, the black dots represent the locations of the hyperbola apexes. The hyperbola apexes are not randomly found along the track of MEX, but they cluster in areas of crustal fields, as shown by Figure 5b.

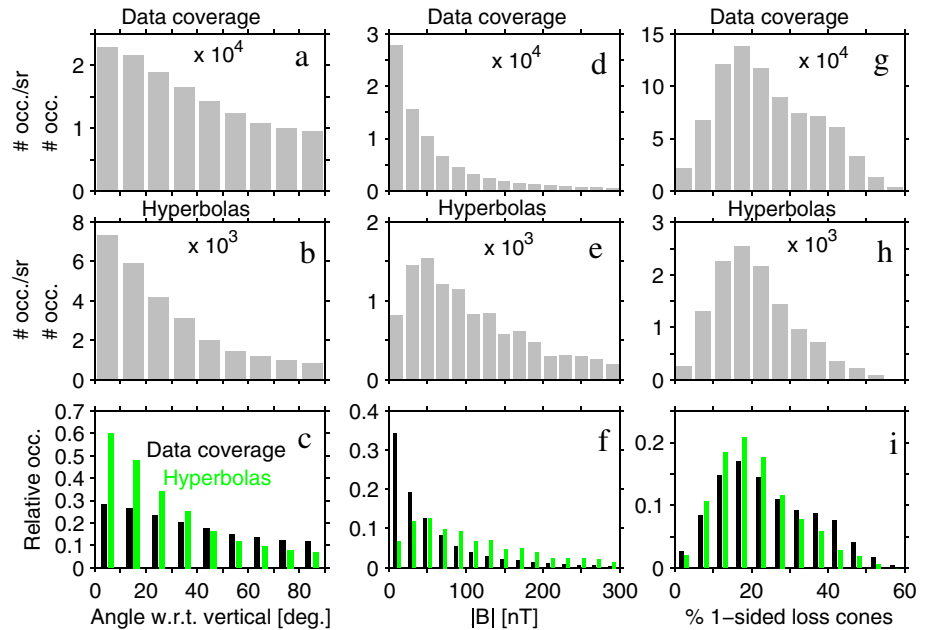
Figure 5b represents the map of the crustal magnetic field strength measured at ~400 km altitude by MGS [Connerney *et al.*, 2001]. The reflector regions are almost all found above the magnetized regions, consistent with the results by Andrews *et al.* [2014] and references therein. They are detected above the strong field regions of the southern hemisphere and also above the moderate fields near the equator. Some outliers are detected outside the magnetic anomalies, possibly indicating that there are weak crustal fields not well captured by the magnetic field observed at ~400 km altitude. Therefore, the formation of density structures occurs at the locations of the magnetic anomalies, for both strong and moderate fields.

Figure 5c shows the map of the magnetic zenith angle of the crustal field measured at ~400 km altitude by MGS [Connerney *et al.*, 2001]. The reflector regions are often found in areas where the field orientation goes from vertical to oblique but tend to avoid horizontal fields, in agreement with results by Andrews *et al.* [2014] and references therein. Therefore, the density structures need magnetic anomalies in order to form but are not located randomly within the minimagnetospheres.

Figure 5d shows the map of the percentage of ~115 eV electron pitch angle distributions indicating a single loss cone observed at ~400 km altitude on the dayside of Mars by MGS [Brain *et al.*, 2007, Figure 11b]. In the unmagnetized regions of the northern hemisphere, the percentage of one-sided loss cone distributions is high, reaching 60% in some places, and indicates that the draped IMF intersects the exobase often and therefore that the solar wind has frequent access to altitudes <400 km; there are only a few reflector regions there. The magnetic anomalies present areas of very low percentage of open field lines (<10%) coinciding with horizontal fields, especially above the strong fields; there are only a few reflector regions there. In contrast, there are some localized areas of moderate percentage of open field lines coinciding with near-vertical to oblique crustal fields (values of 20–40% above moderate fields and up to 50% above strong fields), where the reflector regions tend to cluster. The percentage of one-sided loss cone distributions is lower above the magnetized regions than above the unmagnetized regions (median values of 13% and 28%, for  $|\beta| > 20$  nT and  $|\beta| < 20$  nT, respectively, at 400 km) because the access of the solar wind to the minimagnetospheres depends on the solar wind dynamic pressure and IMF orientation [e.g., Dubinin *et al.*, 2008b; Lillis and Brain, 2013] and is therefore infrequent. The density structures favor neither the regions of low percentage or high percentage of one-sided loss cone distributions, but the regions of moderate percentage instead.

Figure 6 revisits the results from Figure 5 in a more quantitative way, by presenting histograms of the number of ionograms in the data coverage of MARSIS (Figures 6a, 6d, and 6g) and histograms of the number of ionograms for which the hyperbolas lie at or above the surrounding ionosphere (Figures 6b, 6e, and 6h). The black and green histograms in Figures 6c, 6f, and 6i represent the histograms for the data coverage and the hyperbolas, respectively, both normalized to their own number of data points (80,966 and 12,343, respectively). We calculated standard deviations on the number of entries in every bin of the histograms of the number of ionograms with hyperbolas for Figures 6b, 6e, and 6h. We used a binomial error calculation,  $\sigma = \sqrt{N\varepsilon(1-\varepsilon)}$ , where  $N$  is the number of ionograms in the data coverage in these bins and  $\varepsilon$  is the occurrence frequency of detecting the ionograms with hyperbolas in these bins. The errors were typically 2 orders of magnitude smaller than the number of entries in the bins, which made them barely visible in the figure, so we did not plot them here.

Figures 6a–6c correspond to the angle with respect to the vertical of the crustal field model of Cain *et al.* [2003] evaluated at 150 km altitude at the footprint of MEX. Here the polarity of the radial component of the magnetic field has been eliminated by transforming the magnetic zenith angle into the angle of the vector field with respect to the vertical, i.e., between 0° and 90°. The number of occurrences is weighted by the solid angle sustained by the corresponding angle with respect to the vertical, in the same way as Duru *et al.* [2006]. Concerning the weighted distributions of the angle of the field with respect to the vertical,



**Figure 6.** (a–c) Histograms of the angle with respect to the vertical at the location of MEX footprint, calculated at 150 km altitude from the crustal magnetic field model of *Cain et al.* [2003]. The bins are centered from 5° to 85° with steps of 10°. The numbers of occurrences are divided by the solid angle sustained by the associated angle with respect to the vertical, similar to the work by *Duru et al.* [2006] (Figures 6a and 6b). (d–f) Histograms of the field strength at the location of MEX footprint, calculated at 150 km altitude from the crustal magnetic field model of *Cain et al.* [2003]. The bins are centered from 10 nT to 290 nT with steps of 20 nT. (g–i) Histograms of the percentage of ~115 eV electrons one-sided loss cone pitch angle distributions at the location of MEX footprint, measured at ~400 km altitude on the dayside of Mars by MGS, from *Brain et al.* [2007]. The bins are centered from 2.5° to 87.5° with steps of 5°. Figures 6a, 6d, and 6g are for the ionograms of the MARSIS data coverage. Figures 6b, 6e, and 6h are for the ionograms for which the density structures stay at or above the surrounding ionosphere. Figures 6c, 6f, and 6i show the histograms normalized to their own number of samples, for the data coverage (black) and the hyperbolae (green).

the 25th, 50th, and 75th percentiles for the oblique echoes are 4°, 15°, and 34°, respectively (Figure 6b). For both the oblique echoes and the data coverage, the number of ionograms per steradian is largest for small angles (near-vertical fields) and decreases as the angle increases toward the horizontal; however, the decrease is more abrupt for the oblique echoes. This result is consistent with the finding by *Duru et al.* [2006], which used a smaller data set. Finally, Figure 6c shows that the density structures are relatively more frequent than the data coverage for angles <45° and relatively less frequent for angles >45°.

Figures 6d–6f correspond to the strength of the crustal field model of *Cain et al.* [2003] evaluated at 150 km altitude at the footprint of MEX. For the data coverage, the number of ionograms is the largest for low fields and rapidly decreases as the field strength increases (Figure 6d). This can be understood as the fact that vast areas of Mars are weakly magnetized. For the oblique echoes, the number of ionograms is not the largest for low fields but instead peaks at the bin covering 40–60 nT and then decreases slowly as the field strength increases (Figure 6e); the 25th, 50th, and 75th percentiles are 50 nT, 96 nT, and 187 nT. The larger proportion of density structures for moderate fields than for strong fields is due to the fact that more ionograms were acquired over the moderate fields than over the strong fields (Figure 6d). Finally, Figure 6f shows that the density structures are relatively less frequent than the data coverage for  $|B| < 50$  nT and relatively more frequent for  $|B| > 50$  nT.

Figures 6g–6i correspond to the percentage of one-sided loss cone electron distributions from Figure 5d, whose spatial resolution is  $1^\circ \times 1^\circ$ : the percentage value in a given spatial bin was assigned to all ionograms recorded when MEX was located in that bin. In Figure 6g, the distribution peaks at the bin covering 15–20% (considered as a moderate value) and then the number of ionograms decreases as the percentage of one-sided loss cone distributions increases, but the decrease is rather slow and exhibits a plateau shape between percentage values of 27% and 42%. It is the population of high percentage values in the unmagnetized northern hemisphere

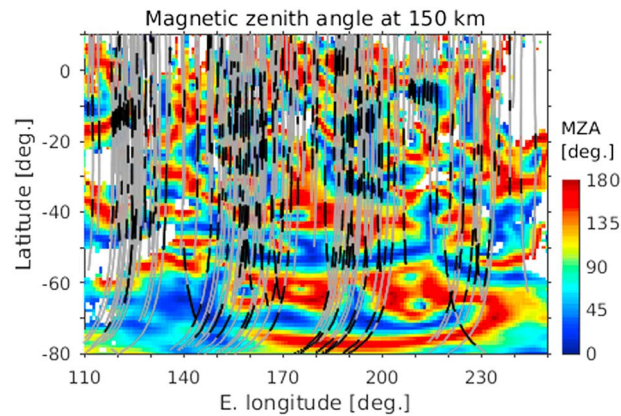


**Figure 7.** Map of the magnetic zenith angle of the crustal magnetic field model of *Cain et al.* [2003], calculated at 150 km altitude, for the region of the strongest fields. The grey curves indicate the footprint of MEX during the MARSIS data coverage. The black curves indicate the footprint of MEX for the time intervals during which the hyperbola traces stay at or above the surrounding ionosphere trace (from Figure 4b).

which causes the plateau shape of the distribution of the total coverage. In Figure 6h, the 25th, 50th, and 75th percentiles of the histogram for the oblique echoes are 13%, 19%, and 27%, respectively. The histogram peaks at the bin covering percentage values of 15–20%, like the data coverage does, and then the number of ionograms decreases rapidly as the percentage of one-sided loss cone distributions increases. Finally, Figure 6i shows that the density structures are relatively more frequent than the data coverage for percentage values between 5% and 30% and are relatively less frequent for percentage values  $>30\%$  and values  $<5\%$ . After having confirmed the role that the magnetic anomalies play in the occurrence of the density structures, we propose to check for a possible influence on the sizes of these structures.

In Figure 7, the locations for which the hyperbolas were found lying at or above the surrounding ionospheric trace (black lines) have been superposed on the map of the magnetic zenith angle of the crustal field model of *Cain et al.* [2003], evaluated at 150 km altitude. The MEX footprints for the MARSIS data coverage during these orbits are also shown as grey lines. The map here focuses on the area of the southern hemisphere where the strong magnetic anomalies are located. One sees several groups of grey lines corresponding to different periods of successive MEX passes over particular geographic regions. *Gurnett et al.* [2005], *Duru et al.* [2006], and *Andrews et al.* [2014] reported that the oblique echoes were recurring over several successive passes, each pass at a nearly fixed longitude separated by a few days, above given near-radial field areas with several degrees width in longitude. Indeed, this is what we see in Figure 7, for example, the cluster of oblique echoes above a downward oriented near-radial field structure (red color) between latitudes  $-8^\circ$  and  $-18^\circ$  and between east longitudes  $112^\circ$  and  $128^\circ$ . From Figure 7, we note that the latitudinal extent for which the reflector regions lie at or above the surrounding ionosphere matches quite well with the latitudinal extent of the near-radial field structures where they are located. We also get this overall impression from the areas of moderate crustal fields (not shown).

We investigate this trend further in Figure 8. Figure 8a represents a latitudinal slice of the crustal magnetic field model of *Cain et al.* [2003] evaluated at 150 km altitude, taken in this example at fixed east longitude =  $199.5^\circ$ . The black curve is the MZA (magnetic zenith angle), and the colored dots indicate the strength of the field at latitude steps of  $1^\circ$ . At this particular longitude, one sees the weak fields of the northern hemisphere and the strong fields of the southern hemisphere. The MZA profile indicates an alternation of minima and maxima in between which the curve intersects several times the vertical dashed line which marks  $MZA = 90^\circ$ ; in other words, there is an alternation of oblique or near-radial fields of opposite polarities (oriented upward or downward), delimited by horizontal fields which form the top of the magnetic arcades.

The locations of the ionograms, during which the hyperbolas lie at or above the surrounding ionosphere trace and which were detected between  $199^\circ$  and  $200^\circ$  east longitude with a longitudinal extent negligible compared to their latitudinal extent, are marked on Figure 8a by vertical red segments placed for convenience at  $MZA = 90^\circ$ . In addition, the locations of the ionograms for the MARSIS data coverage of the associated MEX orbits, for which the longitude of the spacecraft track was between  $199^\circ$  and  $200^\circ$  east longitude, are represented by vertical black segments, also conveniently placed at  $MZA = 90^\circ$ . The density structures are usually located in areas of near-radial or oblique fields, and these are the ones we will consider in order to determine the latitudinal extent of the magnetic regions of a given polarity which best matches with the latitudinal extent of these density structures. The latitudinal extent of these regions is determined by taking the intersections of the MZA profile with the  $MZA = 90^\circ$  line. This is the case for example for the region of upward polarity between latitudes  $-48^\circ$  and  $-56^\circ$  with one extremum at  $MZA = 1^\circ$ . Another example is for

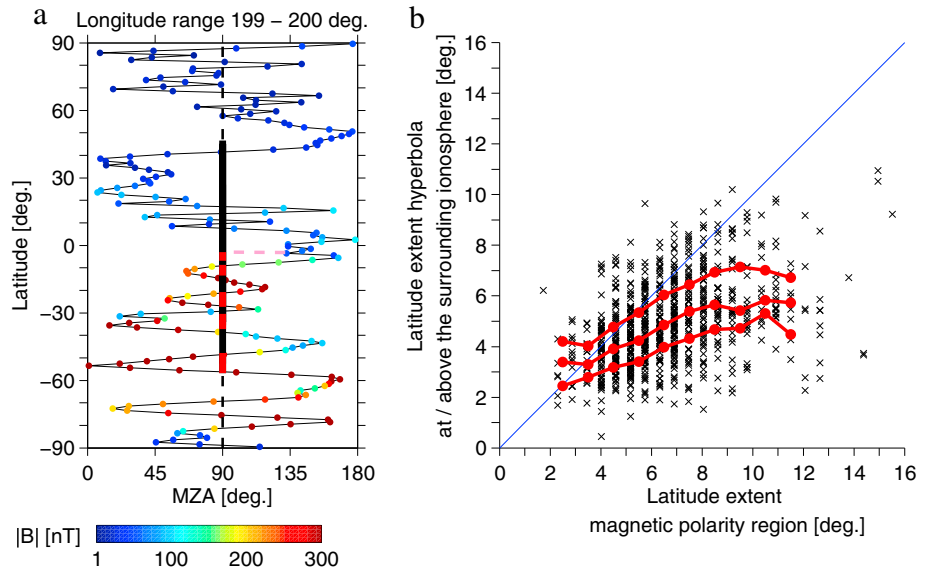


**Figure 8.** (a) Latitude profile of the magnetic zenith angle of the crustal field calculated at 150 km altitude from the model of *Cain et al.* [2003] at east longitude = 199.5° (black curve). The color coding of the circles is the corresponding magnetic field strength at latitude steps of 1°. The dashed vertical black line indicates a horizontal field (MZA = 90°). The vertical red segments represent the latitudinal extent of the hyperbola traces at or above the surrounding ionosphere trace between 199° and 200° east longitude; we excluded from this analysis the hyperbolas whose extents cover several magnetic structures of opposite polarities (not displayed). The pink horizontal dashed line at constant latitude of -3.5° extending between MZA = 90° and 133° marks the edge of the latitudinal extent of the magnetic polarity region chosen to best match the latitudinal extent of the associated density structure (red segment from latitudes -3° to -7°). The vertical black segments represent the latitudinal extent for the MARSIS data coverage for the orbits corresponding to the selected hyperbolas between 199° and 200° east longitude. (b) Scatterplot of the latitudinal extent of the associated best matching magnetic polarity regions versus the latitudinal extent of the hyperbola traces during which they stay at or above the surrounding ionosphere trace (black crosses). The 25th, 50th, and 75th percentiles of the latitude extent of the density structures are indicated by red curves (in ascending order from the bottom of the plot) and calculated in intervals of 1°. The blue straight line indicates the linear function  $y = x$ .

the region of upward polarity between latitudes -29° and -38° with two local extrema at MZA = 15° and 22°. The method needs to be adapted for cases where the latitudinal extent of the density structure is much smaller than the full latitudinal extent of the magnetic region. An example is the region of downward polarity between latitudes 7° and -9° (across the equator) with three local extrema at MZA = 168°, 149°, and 178°. Here the reflector region with a latitudinal extent from -3° to -7° seems to correspond to the extremum at MZA = 168°. We then take the latitudinal extent around this extremum, from latitudes -3.5° (marked by the horizontal pink dashed line in the figure) to -9°. We repeat the procedure for latitudinal slices at all longitudes. We excluded from the analysis the minority of density structures whose apex is located in an area of horizontal crustal fields, which in practice excludes the density structures for which the latitudinal extent covers multiple regions of opposite polarities. It can happen that the latitudinal extents of the density structures cover most of a region of given magnetic polarity and then also partially cover the next region of opposite polarity. These cases are tolerated as long as it is clear to which magnetic polarity region the oblique echoes belong. The procedure left 811 hyperbolas for which we could determine the latitudinal extent of the best matching magnetic polarity regions.

Figure 8b shows a scatterplot of the latitudinal extent of the best matching magnetic polarity regions versus the latitudinal extent during which the hyperbolas lie at or above the surrounding ionosphere trace. The red curves are the median and quartiles of the distribution of the latitude extents of the density structures, calculated in steps of 1°. There are 655 out of 811 hyperbolas (81% of the cases) located below the blue line marking the linear function  $y = x$ , i.e., the cases where the latitudinal extents of the density structures are smaller than the latitudinal extents of the associated magnetic polarity regions. The remaining 156 cases correspond to situations where the density structures were accepted as long as it was clear to which magnetic structure they belonged to, as explained in the previous paragraph. There is a weak positive linear relationship

**Table 1.** Distribution of the SW Index for Various Time Intervals Around the Times of Hyperbola Apexes

Index	$\pm 30$ s		$\pm 1$ min		$\pm 2$ min	
	Number	%	Number	%	Number	%
SW = 0	366	48.1	344	45.2	315	41.4
SW = 1	395	51.9	417	54.8	446	58.6
All	761	100	761	100	761	100

between the sizes of the density structures and the sizes of the associated magnetic polarity regions, with a Pearson linear correlation coefficient of 0.43. The  $p$  value for testing the hypothesis of no correlation against the alternative that there is a nonzero correlation gives  $1.75 \cdot 10^{-37}$ , which is significant at the 5% level. This trend is visible despite a large scatter of points both in the scatterplot and in the increase of the median and quartiles. As the size of the magnetic structure increases, however, the sizes of the reflector regions do not increase as fast: the median and quartiles curves, although increasing overall, move lower compared to the  $y = x$  line. The sizes of the density structures saturate for large magnetic structures with latitude extents  $> 11^\circ$ . There are less statistics for large magnetic structures, so we did not continue the calculation of median and quartiles beyond this limit of  $11^\circ$ . This saturation effect may occur if the density structures have a natural upper limit to their latitudinal extents, which would be dictated by their formation process. This effect may be checked in a future work using the corrected electron density profiles. Another possibility is that inaccuracies of the Cain model downward continued to low altitude may be responsible for producing “too wide” modeled magnetic structures.

### 3.3. Comparison With ASPERA-3/ELS Measurements

Previous studies of the MARSIS oblique echoes [Andrews *et al.*, 2014, and references therein] suggested that the density structures found in areas of near-radial fields may be caused by heating and inflation of the atmosphere resulting from the energy deposition by precipitating electrons.

We will examine the in situ plasma conditions measured by ELS at the location of MEX within time intervals ( $\pm 30$  s,  $\pm 1$  min, and  $\pm 2$  min), around the times that MARSIS detects the apex of the hyperbola traces. We return one more time to the case study of Figure 3 during orbit 4198, to present the method. Figure 3c shows the electron energy time spectrogram from ELS. These time intervals are delimited by vertical dashed lines in Figure 3c:  $\pm 30$  s (black),  $\pm 1$  min (blue), and  $\pm 2$  min (red). At first, the spacecraft was in the magnetosheath, recognized by high fluxes of electrons of energies above 40 eV. At  $\sim 04:07:00$  UT, the decrease in the shocked solar wind flux corresponds to the crossing of the induced magnetosphere boundary. The crossing of the photoelectron boundary at  $\sim 04:07:30$  UT marks the entry into the ionosphere, identified by low fluxes of electrons above 60 eV and by the intense  $\text{CO}_2$  photoelectron peaks at  $\sim 20\text{--}30$  eV [e.g., Frahm *et al.*, 2006a]. We call “boundary layer” the region between the induced magnetosphere boundary and the photoelectron boundary. We already see a variety of situations for the hyperbolas on orbit 4198: the apexes at 04:05:00 UT, 04:07:30 UT, and 04:10:30 UT, for which MEX is respectively located in the magnetosheath, at the induced magnetosphere boundary, and in the ionosphere.

We return to the list of 1066 hyperbolas whose apexes are at the same level or above the surrounding ionosphere trace, and we find 761 hyperbolas for which ELS data were available in the proper instrumental mode within the time intervals requested. The MARSIS data coverage for the orbits corresponding to this selection of oblique echoes comprises 55,115 ionograms. We look for two spectral features during the time intervals around the apex times, and we define two associated indices to classify the density structures. One feature is the presence (absence) of ionospheric photoelectron peaks, corresponding to the photoelectron peak index  $PP = 1$  ( $PP = 0$ ). The other feature is the presence (absence) of solar wind-type distributions, corresponding to the solar wind index  $SW = 1$  ( $SW = 0$ ). There are three categories possible: ionosphere only ( $PP = 1$  and  $SW = 0$ ), solar wind only ( $PP = 0$  and  $SW = 1$ ), or both present ( $PP = 1$  and  $SW = 1$ ). By doing this classification, we will determine which category of plasma conditions is most common at the position of MEX at the times it flies over the reflection regions and thus test the hypothesis that atmospheric heating from solar wind precipitation is necessary to generate the density structures.

First, we look at the distributions of each index and how it changes for the different time intervals we took. Table 1 contains information for the SW index, for  $\pm 30$  s,  $\pm 1$  min, and  $\pm 2$  min intervals. Table 2 contains information for the PP index, in the same format as Table 1.

**Table 2.** Distribution of the PP Index for Various Time Intervals Around the Times of Hyperbola Apexes

Index	$\pm 30$ s		$\pm 1$ min		$\pm 2$ min	
	Number	%	Number	%	Number	%
PP = 0	234	30.75	195	25.6	172	22.6
PP = 1	527	69.25	566	74.4	589	77.4
All	761	100	761	100	761	100

From these tables, we see that for both solar wind-type spectra and photoelectron peak spectra, it makes sense that it is increasingly likely to detect these spectral features (index = 1) for increasing time intervals and increasingly unlikely to not detect these features (index = 0) for increasing time intervals. For example, for the SW index, SW = 0 for 366 cases for  $\pm 30$  s intervals, SW = 0 for 315 cases for  $\pm 2$  min intervals, SW = 1 for 395 cases for  $\pm 30$  s intervals, and SW = 1 for 446 cases for  $\pm 2$  min intervals.

For the three types of time intervals, we see from Tables 1 and 2 that, first, both the solar wind-type spectra and the photoelectron peak spectra are more often detected than they are not detected (numbers for index = 1 are larger than numbers for index = 0). Second, the photoelectron peak spectra are detected more often than solar wind-type spectra are detected (numbers for PP = 1 are larger than numbers for SW = 1). Third, the photoelectron peak spectra are not detected less often than solar wind-type spectra are not detected (numbers for PP = 0 are smaller than numbers for SW = 0). For example, for the  $\pm 2$  min intervals, SW = 1 for 446 cases and SW = 0 for 315 cases, and PP = 1 for 589 cases and PP = 0 for 172 cases. The trends for the PP index and SW index do not change significantly when the duration of the time interval is varied, which allows us to simplify the analysis by considering only one type of time intervals for the rest of the study. We choose  $\pm 2$  min intervals. The oblique echoes are then classified into three categories: ionosphere only (PP = 1 and SW = 0), solar wind only (PP = 0 and SW = 1), or both present (PP = 1 and SW = 1). We will look at examples for each of these categories.

Figure 9 shows time series organized in two columns: one case for PP = 1 and SW = 0 (Figures 9a–9d) and one case for PP = 0 and SW = 1 (Figures 9e–9h). Figures 9a and 9e show the ASPERA-3/ELS electron time spectrogram

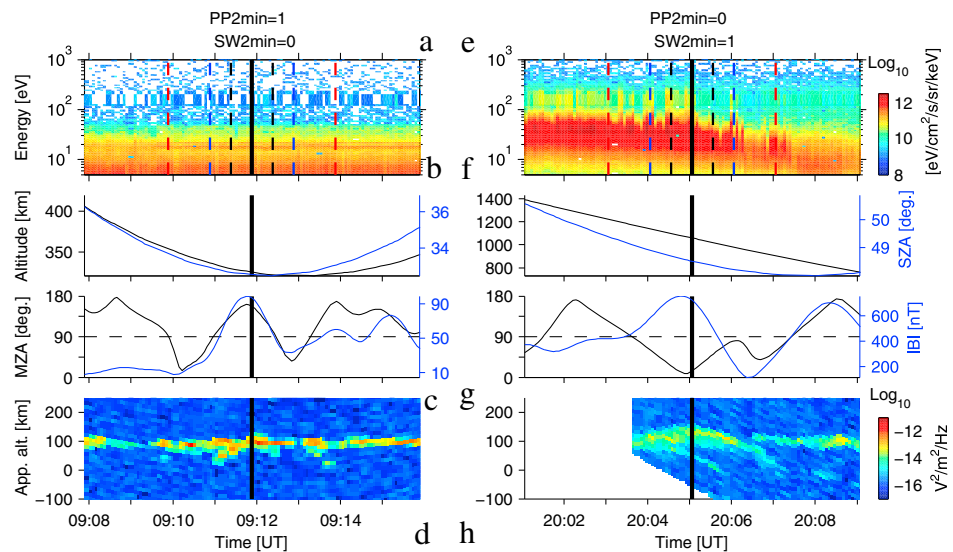


**Figure 9.** Time series for examples of hyperbola traces. The black vertical solid line in all panels marks the time of the hyperbola apex. (a, e) ELS electron energy time spectrogram; the vertical dashed lines have the same meaning as in Figure 3c. (b, f) Position of MEX; left axis: altitude (black); right axis: SZA (blue). (c, g) Crustal magnetic field model [Cain *et al.*, 2003] calculated at 150 km altitude at the footprint of MEX in same format as Figure 3b. (d, h) MARSIS echogram averaged over 1.8–2 MHz. Figures 9a–9d: orbit 3231, example of hyperbola trace with PP = 1 and SW = 0, i.e., with ionospheric spectra only and no solar wind electrons during the  $\pm 2$  min interval around the hyperbola apex time. Figures 9e–9h: orbit 2011, example of hyperbola trace with PP = 0 and SW = 1, i.e., with solar wind spectra only and no ionospheric electrons during the  $\pm 2$  min interval around the hyperbola apex time.

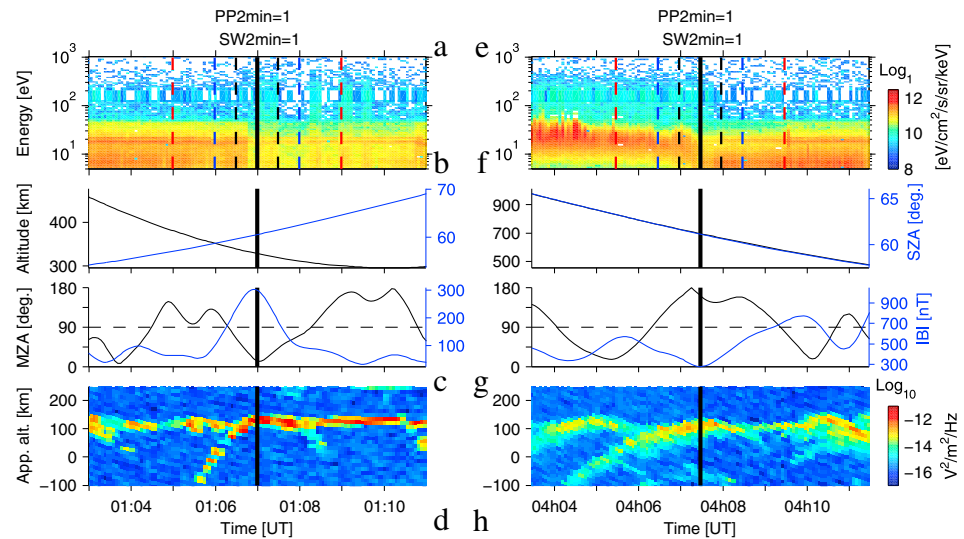


**Figure 10.** Same format as Figure 9. Examples of hyperbola traces with PP = 1 and SW = 1, i.e., with both solar wind and photoelectron peaks present during the ±2 min interval around the hyperbola apex time. (a–d) Orbit 2001, example of solar wind electron spikes in the ionosphere. (e–h) Orbit 4198, example of boundary crossing.

in omnidirectional differential energy flux averaged over sectors 2 to 11. The vertical dashed lines mark the time intervals (black: ±30 s, blue: ±1 min, and red: ±2 min) around the time of the hyperbola apex, itself marked by a thick black vertical line in all panels. Figures 9b and 9f show the position of MEX: the altitude (black curve, left axis) and the solar zenith angle (SZA) (blue curve, right axis). Figures 9c and 9g show the magnetic field model of *Cain et al.* [2003] evaluated at 150 km altitude at MEX footprint: the MZA (black curve, left axis) and the field strength (blue curve, right axis). Figures 9d and 9h show the MARSIS echogram averaged over 1.8–2 MHz.

The example for PP = 1 and SW = 0 is taken on 16 August 2006 during orbit 3231, with the apex of the hyperbola at 09:11:52 UT. The time series runs from 09:08:00 UT to ~09:16:00 UT. In Figure 9d, the hyperbola of interest here has an apparent altitude of 123 km at the apex, with a vertical extent  $\Delta h = 13$  km above the surrounding ionosphere trace. In Figure 9c, at 150 km altitude at the position of apex, the field strength was moderate ( $|B| = 94$  nT) and was near radial, pointing downward (MZA = 157°). In Figure 9b, the spacecraft at that time was located at SZA = 33° and altitude = 352 km. Finally, in Figure 9a, we see CO<sub>2</sub> photoelectron peaks (thick horizontal line at 20–30 eV) but no solar wind-type spectra, for the whole duration of the time series; therefore, MEX was in the ionosphere during all this time.

The example for PP = 0 and SW = 1 is taken on 8 August 2005 during orbit 2011, with the apex of the hyperbola at 20:05:03 UT. The time series runs from 20:01:00 UT to ~20:09:00 UT. In Figure 9h, the hyperbola of interest here has an apparent altitude of 163 km at the apex, with a vertical extent  $\Delta h = 42$  km above the surrounding ionosphere trace. In Figure 9g, at 150 km altitude at the position of apex, the field strength was strong ( $|B| = 715$  nT) and was near radial, pointing upward (MZA = 12°). In Figure 9f, the spacecraft at that time was located at SZA = 48° and altitude = 1057 km. Finally, in Figure 9e, we see that at the beginning the spacecraft was located in the magnetosheath, recognized by large fluxes of electrons with energies >40 eV. The fluxes decrease gradually from 20:05:00 UT, when MEX crosses the induced magnetosphere boundary, and then flies in the boundary layer until 20:09:00 UT. No CO<sub>2</sub> photoelectron peaks are observed for the whole time series.

In the same format as Figure 9, Figure 10 now shows time series in two columns for two examples of oblique echoes with PP = 1 and SW = 1. The situations are varied for this category, so we examine two quite different cases.

Figures 10a–10d show one case taken on 6 August 2005 during orbit 2001, with the apex of the hyperbola at 01:07:00 UT. The time series runs from 01:03:00 UT to 01:11:00 UT. In Figure 10d, the hyperbola of interest here has an apparent altitude of 165 km at the apex, with a vertical extent  $\Delta h = 41$  km above the surrounding ionosphere trace. In Figure 10c, at 150 km altitude at the position of apex, the field strength was strong ( $|B| = 295$  nT) and was near radial, pointing upward (MZA = 12°). In Figure 10b, the spacecraft at that time

**Table 3.** Classification of Oblique Echoes According to the Presence or Absence of Solar Wind (SW) Type Spectra and of CO<sub>2</sub> Photoelectron Peaks (PP) in the ELS Data During Intervals of ±2 Min Around the Times of Hyperbola Apexes

Group	PP = 1 SW = 0	PP = 0 SW = 1	PP = 1 SW = 1	All
Number	315	172	274	761
%	41.3	22.6	36.1	100

was located at SZA = 61° and altitude = 329 km. Finally, in Figure 10a, we see CO<sub>2</sub> photoelectron peaks for the whole time series, indicating that MEX was in the ionosphere. Meanwhile, several spikes of enhanced electron fluxes ranging from 5 eV to 300 eV are seen from 01:05:00 UT to 01:06:00 UT, from 01:08:15 UT to 01:08:30 UT, from 01:09:00 UT to

01:09:15 UT, and from 01:09:30 UT to 01:09:45 UT. The plasma in these spikes presents a mixture of ionospheric characteristics (photoelectron peaks) and solar wind characteristics (high fluxes at high energies), suggesting that it comes from the boundary layer. These spikes are not associated with structures in the crustal fields (Figure 10c) and suggest a disturbance of the plasma boundaries by Kelvin-Helmholtz instabilities [e.g., Gurnett *et al.*, 2010]. One spike was observed within both ±30 s and ±1 min time intervals (and occurs at the time of the hyperbola apex), and an additional spike is seen during the ±2 min time interval.

Figures 10e–10h show one case taken on 13 April 2007 during orbit 4198, with the apex of the hyperbola at 04:07:30 UT. Note that we previously examined this case in Figures 1 and 3. The time series runs from ~04:03:30 UT to ~04:11:30 UT. In Figure 10h, the hyperbola of interest here has an apparent altitude of 145 km at the apex, with a vertical extent Δ*h* = 22 km above the surrounding ionosphere trace. In Figure 10g, at 150 km altitude at the position of apex, the field strength was strong (*|B|* = 279 nT) and was near radial, pointing downward (MZA = 163°). In Figure 10f, the spacecraft at that time was located at SZA = 61° and altitude = 693 km. Finally, in Figure 10e, we see that at the beginning MEX was located in the magnetosheath and then crossed the induced magnetosphere boundary at ~04:07:00 UT, traveled in the boundary layer until ~04:07:30 UT, and then entered the ionosphere afterward. Here the three intervals all contain a single boundary crossing (from solar wind to ionosphere).

Table 3 gives the distributions of the three categories of pairs of SW and PP indices for the ±2 min intervals. Out of 761 cases, 41.3% correspond to SW = 0 and PP = 1 (ionosphere only), 22.6% correspond to SW = 1 and PP = 0 (solar wind only), and 36.1% correspond to SW = 1 and PP = 1 (both ionosphere and solar wind). In order to interpret the observations of these three categories, it is instructive to know the altitude and SZA of MEX at these times.

Figure 11a shows the MARSIS data coverage for the locations of the spacecraft in bins of 10° in SZA and 50 km in altitude, with the color coding giving the number of ionograms in each bin. The thick black curve marks the position of the induced magnetosphere boundary model by *Dubinin et al.* [2006]. The data coverage was restricted to MEX altitude < 1100 km and MEX SZA < 90°. The coverage is better for SZA > 20° and altitude < 700 km.

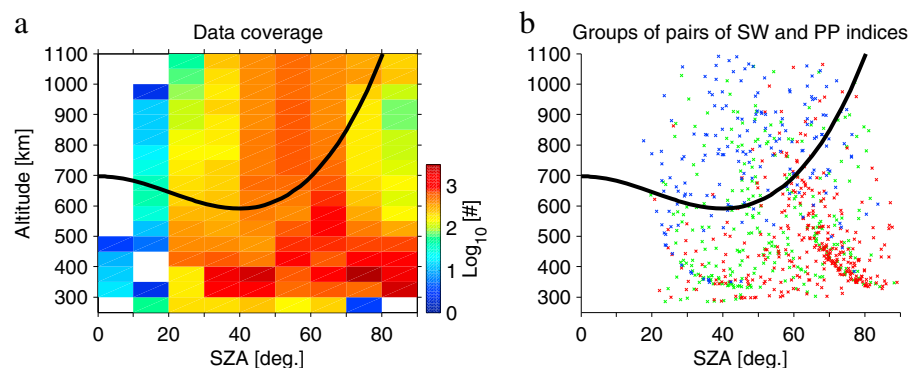


**Figure 11.** (a) Number of ionograms of the MARSIS data coverage, as a function of MEX altitude and SZA. (b) Locations of hyperbola apexes colored by category of plasma conditions (pairs of SW and PP indices), as a function of MEX altitude and SZA. Categories: PP = 1 and SW = 1 (green), PP = 0 and SW = 1 (blue), and PP = 1 and SW = 0 (red). In both panels, the thick black curve marks the induced magnetosphere model by *Dubinin et al.* [2006].

Figure 11b shows the locations of the hyperbola apexes, in the same axes. The color of the dots indicates the category of plasma conditions measured by ELS during the  $\pm 2$  min intervals around the apex times: SW = 1 and PP = 1 (green), SW = 1 and PP = 0 (blue), and SW = 0 and PP = 1 (red). The majority of the SW = 1 and PP = 0 cases (solar wind only) are found at high altitude and above the induced magnetosphere model curve. Then the majority of the SW = 0 and PP = 1 cases (ionosphere only) are found at low altitudes and below the model curve. Finally, the SW = 1 and PP = 1 cases (both solar wind and ionosphere) are found somewhere in between, distributed equally above or below the model curve. Some cases with solar wind-only (ionosphere-only) plasmas are found below (above) the average altitude of the boundary, which may be explained by the varying upstream dynamic pressure. These trends make sense given what we know of the positions of the plasma domains relative to Mars [e.g., *Dubin et al., 2006*].

#### 4. Discussion

The present work uses the list of 1126 dayside electron density structures identified by *Andrews et al. [2014]* in the active ionospheric sounding data measured by the MARSIS onboard MEX. We selected 1066 density structures whose apex was lying at or above the surrounding ionosphere on the same isodensity contour (chosen as  $4.47 \cdot 10^4 \text{ cm}^{-3}$ ), corresponding to cases where MEX flew right over or very near these structures, for further analysis.

The width of the reflector regions increases when their vertical extent increases (Figure 4e). Furthermore, they are much wider than they are high: the median extent along MEX footprint during which the hyperbolas stay at or above the surrounding ionosphere is 347 km (Figure 4c), compared to a median vertical extent of 18 km above the surrounding ionosphere (Figure 4a). From the echograms, the reflector regions appear often like gentle hills, a finding which needs to be confirmed in a future work using the density profiles corrected for dispersion. The latitude extent of the density structures covers several degrees, with a median of  $\sim 5^\circ$  (Figure 4d).

The spacecraft flies over the reflector regions for durations from  $\sim 10$  s to  $\sim 3$  min, with the median time interval of 83 s (Figure 4b). As soon as the density structure is within reflection range from the radar, it shows up as a downward-facing hyperbola in the echogram, with typically one to a few tens of ionograms (7.54 s each) covering each branch of the hyperbola, which means that the duration for which the structure is detected can effectively be at least doubled. It is very likely that these reflector regions existed a significant time before MEX detected them and again a significant time after. This lifetime might be hours, but it is not clear if they could persist after dark or even for several days. The reason is because the nightside topside electron densities are very low, often below the detection threshold of MARSIS, i.e.,  $5000 \text{ cm}^{-3}$ , such that nightside ionospheric reflections, whether vertical or oblique, are not frequently measured [*Němec et al., 2010*]. We do not therefore know whether the density structures do persist for several days, or if they actually disappear during nighttime and reform during daytime. What is certain is that when the density structures do form, they are very stable in their locations: they are frequently detected on the dayside during several consecutive MEX passes above a given geographic area, over periods of tens of days [*Gurnett et al., 2005; Duru et al., 2006; Andrews et al., 2014*].

We have confirmed the relationship between oblique echoes and magnetic anomalies established by previous works [e.g., *Gurnett et al., 2005; Duru et al., 2006*]. The reflection regions are preferentially found above the magnetic anomalies (Figure 5b); they occur on both moderate and strong crustal fields, with a median  $|\mathbf{B}| = 96 \text{ nT}$  at 150 km altitude at the locations of the hyperbola apexes (Figures 6d–6f). They are preferentially found in areas of vertical to oblique crustal fields, avoiding horizontal crustal fields (Figure 5c). The density structures are indeed more frequent in areas where the angle of the crustal field with respect to the vertical is less than  $45^\circ$  (more vertical) than in areas where this angle is greater than  $45^\circ$  (more horizontal); the median angle with respect to the vertical is  $15^\circ$  at 150 km altitude at the locations of the apexes (Figures 6a–6c). Furthermore, the latitudinal extents of the density structures match quite well with the latitudinal extents of the associated “best matching” magnetic polarity region at 150 km altitude (Figure 7) and that the former one tends to increase when the latter one increases, but not as rapidly (Figure 8): these are new results. This means that wider (and therefore higher) density structures tend to be associated with wider regions of given magnetic polarity; however, the latitudinal extents of the structures seem to saturate after  $11^\circ$ . It may indicate a natural upper limit to the extents of the density structures,

coming from their formation process, and/or it may indicate inaccuracies in the Cain model when it is downward continued to 150 km altitude in some areas. In addition, we found no relationship between the latitudinal extents of the reflector regions and the field strength at 150 km altitude (figure not shown).

The strength of the field seems then to be a weak controlling factor, since even the small magnetic anomalies around the equator present density structures and the proportion does not increase when the field strength increases from moderate to strong. So the presence of planetary magnetization matters more than its strength. In contrast, the angle of the crustal field with respect to the vertical exerts a significant control on the reflector regions: directly through the preferred locations and indirectly through their latitudinal extents.

The percentage of one-sided loss cone distributions also tells something about the origin and orientation of the dominant magnetic field in a particular place (Figure 5d). The density structures are relatively more frequent for percentage values between 5% and 30% and are relatively less frequent for percentage values >30% and values <5% (Figures 6g–6i); the median percentage value for the locations of the hyperbolas is 19%. The oblique echoes avoid the areas of high percentage of one-sided loss cone distributions, which happen to be in the weakly magnetized northern hemisphere, where the IMF has easy access to low altitudes and often intersects the exobase. It means that having frequent access of the solar wind to low altitudes is not the mechanism to form the density structures. The oblique echoes also avoid the zones of very low percentage of one-sided loss cone distributions within the magnetic anomalies, which happen to be zones of horizontal crustal fields, with almost always closed field lines and no access from the solar wind. The reflector regions are instead found in the areas of moderate percentage of one-sided loss cone distributions, which happen to be in the regions of near-radial fields within the magnetic anomalies (percentage values from 20% to 50% depending on  $|\beta|$ ) and indicate that the field lines are sometimes open, allowing the access by the solar wind. These structures form repetitively in areas where the solar wind has access or not depending on the magnetic topology: field lines reconnected with the IMF or field lines connected to the distant footprint of opposite magnetic polarity along the same magnetic arcade [e.g., *Krymskii et al.*, 2002]. Therefore, the topology of the crustal field lines (open or not) is not a controlling factor, as long as it is near vertical.

We note that the upstream conditions will vary significantly over the course of the sequences of MEX orbits (around tens of days) selected by *Andrews et al.* [2014], with Mars being exposed to low or high dynamic pressure flows and exposed to “toward Sun” or “away from Sun” IMF sectors. These authors examined a sequence of MEX orbits passing above a particular region, for which there were simultaneous vector magnetic field measurements by MGS/MAG-ER, and found no consistent trends of the occurrence of the density structures during these orbits on the upstream dynamic pressure proxy developed by *Brain et al.* [2005] or on the IMF clock angle proxy developed by *Brain et al.* [2006a]. For completeness, we checked all the orbit sequences from the list of *Andrews et al.* [2014] for which these proxies were available, i.e., for times before November 2006. This leaves us with 31 MEX orbits and 94 oblique echoes. Despite the low statistics, we are able to say that there are no consistent trends in the external conditions for the occurrence of oblique echoes in the areas with multiple MEX passes (figures not shown). The long-term stability of the oblique echoes seems to be consistent with the apparent nondependence on the IMF orientation and solar wind dynamic pressure. This is in contrast with the control exerted by external conditions on the access of suprathermal electrons to 400 km altitude [e.g., *Brain et al.*, 2006b; *Dubin et al.*, 2008b; *Lillis and Brain*, 2013] and with the external control of the percentage of 115 eV electron pitch angle distributions indicating open or closed field lines [*Brain et al.*, 2014].

There are many observational studies reporting suprathermal electrons precipitating in the Martian atmosphere into near-radial crustal fields on the dayside and the nightside [e.g., *Mitchell et al.*, 2001; *Brain et al.*, 2005, 2006b; *Lundin et al.*, 2006; *Soobiah et al.*, 2006; *Dubin et al.*, 2008a, 2008b; *Halekas et al.*, 2008; *Lillis and Brain*, 2013; *Soobiah et al.*, 2013; *Diéval et al.*, 2014]. The resulting patches of ionization on the nightside of Mars have been modeled by, e.g., *Lillis et al.* [2009] and *Fillingim et al.* [2007] and observed by, e.g., *Němec et al.* [2010, 2011].

On the nightside, *Němec et al.* [2010, 2011] made remote measurements of the topside densities using MARSIS and found areas of enhanced ionization located in near-radial crustal fields, in regions of relatively high occurrence frequency of open field line configuration [*Brain et al.*, 2007]. The increased density values were detected up to  $\sim 4 \cdot 10^4 \text{ cm}^{-3}$ , larger than the nightside background density, which is often below the detection threshold of MARSIS for low densities, i.e., below  $5000 \text{ cm}^{-3}$  [*Němec et al.*, 2010]. *Němec et al.*

[2010, 2011] interpreted that the patchy ionosphere was generated by electron impact ionization from solar wind electron precipitation along open field lines formed by magnetic reconnection between the magnetic anomalies and the IMF. This interpretation was supported by the low frequency of observation of these ionospheric patches over repetitive passes of the spacecraft over the same area, indicative of the time dependence of the magnetic reconnection process. Indeed, *Diéval et al.* [2014] reported that cases of very high peak densities detected by MARSIS on the nightside of Mars were often associated to Westward IMF and often simultaneously with accelerated electrons of peak energies  $>100$  eV detected in situ by ASPERA-3, both findings pointing to magnetic reconnection. Similarly, *Safaieinili et al.* [2007] and *Cartacci et al.* [2013] interpreted that electron impact ionization from solar wind precipitation may explain the measurements of enhancements of the ionospheric total electron content in regions of strong near-radial fields, as observed by MARSIS in subsurface mode on the nightside. We note that the cases of measurable peak densities on the nightside were often at too low apparent altitude for being vertical reflections, and their trace often showed up as hyperbola traces in the echograms [*Němec et al.*, 2011; *Diéval et al.*, 2014]. These signatures indicate localized density structures on the nightside, similar to the ones we have examined on the dayside. We mentioned earlier the possibility that the dayside density structures might survive for some time on the nightside, but with densities too low to be detected by MARSIS, due to the electron-ion recombination occurring in the absence of ionizing UV radiation. However, when the external conditions allow for it, the field lines in areas of near-radial fields may become open and solar wind electron precipitation may generate extra ionization and heating at low altitudes. This would reinforce the density structures which may have formed earlier during daytime, by increasing their electron densities to the point of becoming detectable as nightside oblique echoes.

We suggest that solar wind electron precipitation happening during nighttime is able to reinforce ionospheric density structures which were presumably formed during daytime, from the background densities resulting from photoionization of the atmospheric neutrals by UV. But what causes the dayside density structures in the first place? In order to answer this question, we have taken the advantage of the readily available in situ electron distributions measurements made by ASPERA-3 at the altitude of MEX, and we have classified the oblique echoes per category of plasma conditions.

For the 22.6% of cases corresponding to solar wind only, the spacecraft altitude was usually high enough so that it was immersed in the magnetosheath flow for the full  $\pm 2$  min interval, which makes it impossible, in the absence of measured pitch angle distributions, to determine if the solar wind electrons could penetrate to lower altitude below the exobase (i.e., one-sided loss cone distributions) and down to the density structures. To solve this problem, we use the finding that the density structures are found mostly above the magnetized regions [e.g., *Andrews et al.*, 2014, and references therein] and the finding that the minimagnetospheres act to raise the minimum altitude reached by the solar wind plasma and magnetic field [e.g., *Crider et al.*, 2002; *Brain et al.*, 2005; *Fränz et al.*, 2006; *Brain et al.*, 2003]. Therefore, we expect that in these areas the draped IMF is less likely to intersect the collisional atmosphere starting below  $\sim 180$  km altitude, and thus the less likely access by the solar wind.

For the 41.3% of cases corresponding to ionosphere only, the spacecraft altitude was usually low enough such that it was flying in the ionosphere. Note that it is more likely to find ionospheric plasma than solar wind plasma at a given altitude above the magnetized regions, since the magnetic anomalies raise the altitude of the IMB and the altitude of the ionopause [e.g., *Crider et al.*, 2002; *Duru et al.*, 2009]. Finally, the ionospheric plasma contained within the minimagnetospheres usually exhibits fully isotropic pitch angle distributions and also double-loss cone distributions (trapped electrons), both indicative of closed field lines with both ends in the crust [e.g., *Brain et al.*, 2007]. Therefore, the observations of the category with ionospheric plasma only are indications that the solar wind has no access to these field lines.

Finally, for the 36.1% of cases presenting both ionospheric and solar wind plasmas, the spacecraft was crossing one or several times the different plasma domains. These cases comprise situations with single boundary crossing or multiple boundary crossings due to varying upstream dynamic pressure [e.g., *Brain et al.*, 2005; *Dubinin et al.*, 2009], Kelvin-Helmholtz instabilities [e.g., *Gurnett et al.*, 2010], or accelerated/heated electron signatures localized in areas of radial crustal fields [e.g., *Soobiah et al.*, 2013]. We note that the most frequent situations we encountered were single boundary crossing. Multiple crossings were also encountered and were more often extended in time (dynamic pressure changes and Kelvin-Helmholtz instabilities occurring over several minutes)

than localized in time (electron spikes  $< 1$  min). The situations with electron spikes showed more often heated electrons than accelerated electrons, consistent with *Soobiah et al.* [2013]. We did not record the numbers illustrating these different situations, i.e., we did not record whether the solar wind-type spectra and ionospheric spectra were found simultaneously or successively in time, nor if they occurred on radial fields or not, but just if they occurred at all. The exact timing of these spectral features relative to the hyperbola apex time is not considered important since the density structures are not “points” but rather several hundreds of kilometers wide, with measured “durations” of typically 1 to 2 min (Figures 4b and 4c), which are significant compared to the time intervals used in this study:  $\pm 30$  s,  $\pm 1$  min, and  $\pm 2$  min. The boundary layer, which is the region comprised between the magnetosheath and the ionosphere, is detected at every boundary crossing, so it is worth discussing it further. *Frahm et al.* [2006b] reported the presence of photoelectron peak spectra, from the photoelectron boundary and up to the induced magnetosphere boundary. However, this does not imply that the field lines in the boundary layer have access to the peak altitude of photoelectron production (120–140 km on the dayside) below the exobase. *Han et al.* [2014] interpreted that 20–30 eV photoelectrons could diffuse vertically across the induced ionospheric magnetic field, up into the boundary layer, thus reaching higher altitudes than the cold bulk ionospheric photoelectrons (energies  $< 1$  eV) due to larger gyroradii. In the boundary layer, *Crider et al.* [2000] also observed a decrease of the  $> 40$  eV solar wind electron flux, which they attributed to the energy degradation of solar wind electrons by electron impact ionization with atmospheric neutrals. *Crider et al.* [2000] interpreted that the electron impact ionization responsible for the decrease of the energetic solar wind fluxes in the boundary layer occurs primarily in the portion of the draped magnetic flux tubes intersecting the dense neutral atmosphere at low altitudes in the subsolar region. However, this does not imply that these flux tubes intersect the exobase. In particular, the magnetic anomalies will again raise the minimum altitude reached by the solar wind, so we expect that the field lines in the boundary layer (and the solar wind electrons) will not intersect the collisional atmosphere.

In summary, the largest number of cases (41.3%) corresponds to ionospheric plasma only, while the two other categories are unlikely to bring the solar wind to the ionospheric altitudes down to the density structures, because of the special situation of these structures preferring the magnetized regions of Mars. We also recall that the oblique echoes were not found in the weakly magnetized northern hemisphere where the solar wind frequently reaches altitudes below 400 km. It appears that the hypothesis presented by *Gurnett et al.* [2005] does not apply in the majority of cases, i.e., the heating by solar wind electron precipitation is not required for generating the majority of the reflector regions. Although the precipitation sometimes occurs during daytime into magnetic cusps within the magnetic anomalies, it would just help reinforce the density structures previously formed by another more “recurrent” process, which future studies may help identify, in particular with MARSIS remote measurements of density profiles corrected for signal dispersion.

## 5. Summary and Conclusion

A statistical study of topside dayside electron density structures observed in areas of near-radial crustal magnetic fields by the MARSIS onboard MEX led to the following results. The majority of the density structure apexes were found below MEX and to be higher than the surrounding ionospheric density level of  $4.47 \cdot 10^4 \text{ cm}^{-3}$  (median apparent altitude above the surrounding ionosphere = 18 km). The density structures are much wider than they are high, and their height increases when their width increases (median distance = 347 km along the footprint of MEX for which the density structures stay at or above the surrounding ionosphere). They are observed for one to several minutes when the radar is within reflection range (median duration = 83 s for the overhead pass) but last probably much longer. The density structures are found above both moderate and strong magnetic anomalies, but preferentially above near-radial fields (median angle with respect to the vertical =  $15^\circ$  and median strength = 96 nT, for the crustal magnetic field vectors evaluated at 150 km altitude from the Cain model). They have corresponding latitudinal extensions of several degrees (median  $\sim 5^\circ$ ), which are larger for wider structures of given magnetic polarity at 150 km altitude. They are repetitively observed above areas with a moderate percentage value (median = 19%) of one-sided loss cone electron distributions at  $\sim 115$  eV (where there are near-radial crustal fields), over periods of tens of days, despite the control of the magnetic topology by the varying external conditions. Furthermore, the density structures are observed for varying plasma conditions at the altitude of MEX, with the most frequent plasma category (41.3% of cases) showing ionospheric plasma only, indicative of closed field lines, not open field lines. These findings disprove the hypothesis of atmospheric

heating by precipitating solar wind electrons suggested by Gurnett *et al.* [2005]. However, the near-vertical crustal fields are an important controlling factor, so the density structures are able to reform easily, even if these field lines remain connected to the other footprint of the magnetic arcade, rather than reconnected to the IMF. We also suggest that the ion-electron recombination occurring on the nightside lowers the densities of the reflection regions to the point that they fall below the MARSIS detection threshold. However, these density structures would become sometimes detectable on the nightside when intermittent suprathermal electron precipitation brings additional heating and ionization into a newly formed magnetic cusp region.

In order to test the other hypotheses proposed by other authors [Andrews *et al.*, 2014; Matta *et al.*, 2015] to explain the density structures, one would need to know whether the density structures are found at altitudes where the plasma transport dominates or the photochemistry dominates. We plan to do a follow-up statistical study of the corrected density profiles at the times of the density structures, in order to further constrain their nature and causes, beyond what was achieved in the present work, by determining their altitude range and plasma scale heights, and by looking for enhanced peak densities like the ones reported by Nielsen *et al.* [2007b].

The study of the density structures will be greatly enhanced by the in situ measurements of the thermal density, temperature, and energy distributions of the ions, electrons and atmospheric neutrals, the wave activity, and the magnetic field vectors performed by the MAVEN (Mars Atmosphere and Volatile Evolution) spacecraft, in orbit around Mars since September 2014. MAVEN reaches its pericenter nominally at 150 km altitude, and down to 125 km during deep-dip campaigns, so it should observe the density structures on a regular basis whenever it passes above near-radial field regions.

#### Acknowledgments

C.D., D.A.G., and D.D.M. were supported by contract 1224107 by the Jet Propulsion Laboratory. C.D. also acknowledges funding from the Science and Technology Facilities Council (grant ST/M001059/1). D.J.A. was supported by SNSB grant 162/14 and Vetenskapsrådet grant 621-2014-5526. The ASPERA-3 data and the MARSIS data are available on the Planetary Data System website. The upstream IMF clock angle and upstream dynamic pressure proxies developed by Brain *et al.* [2005, 2006a] are available on [www.srpg.ssl.berkeley.edu/~brain/welcome2.html](http://www.srpg.ssl.berkeley.edu/~brain/welcome2.html).

Michael Liemohn thanks Jeremy Rioussset and Kushal Mahajan for their assistance in evaluating the paper.

#### References

- Acuña, M. H., et al. (1999), Global distribution of crustal magnetization discovered by the Mars Global Surveyor MAG/ER experiment, *Science*, 284(5415), 790–793, doi:10.1126/science.284.5415.790.
- Andrews, D. J., M. André, H. J. Opgenoorth, N. J. T. Edberg, C. Diéval, F. Duru, D. A. Gurnett, D. D. Morgan, and O. Witasse (2014), Oblique reflections in the Mars Express MARSIS data set: Stable density structures in the Martian ionosphere, *J. Geophys. Res. Space Physics*, 119, 3944–3960, doi:10.1002/2013JA019697.
- Barabash, S., et al. (2006), The Analyzer of Space Plasmas and Energetic Atoms (ASPERA-3) for the Mars Express Mission, *Space Sci. Rev.*, 126(1–4), 113–164, doi:10.1007/s11214-006-9124-8.
- Brain, D. A., F. Bagenal, M. H. Acuña, and J. E. P. Connerney (2003), Martian magnetic morphology: Contributions from the solar wind and crust, *J. Geophys. Res.*, 108(A12), 1424, doi:10.1029/2002JA009482.
- Brain, D. A., J. S. Halekas, R. Lillis, D. L. Mitchell, R. P. Lin, and D. H. Crider (2005), Variability of the altitude of the Martian sheath, *Geophys. Res. Lett.*, 32, L18203, doi:10.1029/2005GL023126.
- Brain, D. A., D. L. Mitchell, and J. S. Halekas (2006a), Magnetic field draping direction at Mars from April 1999 through August 2004, *Icarus*, 182, 464–473, doi:10.1016/j.icarus.2005.09.023.
- Brain, D. A., J. S. Halekas, L. M. Peticolas, R. P. Lin, J. G. Luhmann, D. L. Mitchell, G. T. Delory, S. W. Bougher, M. H. Acuña, and H. Rème (2006b), On the origin of aurorae on Mars, *Geophys. Res. Lett.*, 33, L01201, doi:10.1029/2005GL024782.
- Brain, D. A., R. J. Lillis, D. L. Mitchell, J. S. Halekas, and R. P. Lin (2007), Electron pitch angle distributions as indicators of magnetic field topology near Mars, *J. Geophys. Res.*, 112, A09201, doi:10.1029/2007JA012435.
- Brain, D. A., et al. (2014), Eighth International Conference on Mars, held July 14–18, 2014 in Pasadena, California. LPI contribution no. 1791, 1394.
- Cain, J. C., B. B. Ferguson, and D. Mozzoni (2003), An  $n = 90$  internal potential function of the Martian crustal magnetic field, *J. Geophys. Res.*, 108(E2), 5008, doi:10.1029/2000JE001487.
- Cartacci, M., E. Amata, A. Cicchetti, R. Nosciese, S. Giuppi, B. Langlais, A. Frigeri, R. Orosei, and G. Picardi (2013), Mars ionosphere total electron content analysis from MARSIS subsurface data, *Icarus*, 223(1), 423–437, doi:10.1016/j.icarus.2012.12.011.
- Connerney, J. E. P., M. H. Acuña, P. J. Wasilewski, and G. Kletetschka (2001), The global magnetic field of Mars and implications for crustal evolution, *Geophys. Res. Lett.*, 28(21), 4015–4018, doi:10.1029/2001GL013619.
- Crider, D. H., et al. (2000), Evidence of electron impact ionization in the magnetic pileup boundary of Mars, *Geophys. Res. Lett.*, 27(1), 45–48, doi:10.1029/1999GL003625.
- Crider, D. H., et al. (2002), Observations of the latitude dependence of the location of the Martian magnetic pileup boundary, *Geophys. Res. Lett.*, 29(8), 1170, doi:10.1029/2001GL013860.
- Detrick, D. L., T. J. Rosenberg, and C. D. Fry (1997), Analysis of the Martian atmosphere for riometry, *Planet. Space Sci.*, 45(3), 289–294, doi:10.1016/S0032-0633(96)00134-1.
- Diéval, C., D. D. Morgan, F. Nemeč, and D. A. Gurnett (2014), MARSIS observations of the Martian nightside ionosphere dependence on solar wind conditions, *J. Geophys. Res. Space Physics*, 119, 4077–4093, doi:10.1002/2014JA019788.
- Dubinin, E., M. Franz, J. Woch, E. Roussos, S. Barabash, R. Lundin, J. D. Winningham, R. A. Frahm, and M. Acuña (2006), Plasma morphology at Mars: ASPERA-3 observations, *Space Sci. Rev.*, 126(1–4), 209–238, doi:10.1007/s11214-006-9039-4.
- Dubinin, E., M. Fraenz, J. Woch, J. D. Winningham, R. Frahm, R. Lundin, and S. Barabash (2008a), Suprathermal electron fluxes on the nightside of Mars: ASPERA-3 observations, *Planet. Space Sci.*, 56(6), 846–851, doi:10.1016/j.pss.2007.12.010.
- Dubinin, E., M. Fraenz, J. Woch, E. Roussos, J. D. Winningham, R. A. Frahm, A. Coates, F. Leblanc, R. Lundin, and S. Barabash (2008b), Access of solar wind electrons into the Martian magnetosphere, *Ann. Geophys.*, 26, 3511–3524, doi:10.5194/angeo-26-3511-2008.
- Dubinin, E., M. Fraenz, J. Woch, F. Duru, D. Gurnett, M. Ronan, S. Barabash, and R. Lundin (2009), Ionospheric storms on Mars: Impact of the corotating interaction region, *Geophys. Res. Lett.*, 36, L01105, doi:10.1029/2008GL036559.

- Duru, F., D. A. Gurnett, T. F. Averkamp, D. L. Kirchner, R. L. Huff, A. M. Persoon, J. J. Plaut, and G. Picardi (2006), Magnetically controlled structures in the ionosphere of Mars, *J. Geophys. Res.*, *111*, A12204, doi:10.1029/2006JA011975.
- Duru, F., D. A. Gurnett, R. A. Frahm, J. D. Winningham, D. D. Morgan, and G. G. Howes (2009), Steep, transient density gradients in the Martian ionosphere similar to the ionopause at Venus, *J. Geophys. Res.*, *114*, A12310, doi:10.1029/2009JA014711.
- Fillingim, M. O., L. M. Peticolas, R. J. Lillis, D. A. Brain, J. S. Halekas, D. L. Mitchell, R. P. Lin, D. Lummerzheim, S. W. Bougher, and D. L. Kirchner (2007), Model calculations of electron precipitation induced ionization patches on the nightside of Mars, *Geophys. Res. Lett.*, *34*, L12101, doi:10.1029/2007GL029986.
- Fillingim, M. O., L. M. Peticolas, R. J. Lillis, D. A. Brain, J. S. Halekas, D. Lummerzheim, and S. W. Bougher (2010), Localized ionization patches in the nighttime ionosphere of Mars and their electrodynamic consequences, *Icarus*, *206*(1), 112–119, doi:10.1016/j.icarus.2009.03.005.
- Fillingim, M. O., R. J. Lillis, S. L. England, L. M. Peticolas, D. A. Brain, J. S. Halekas, C. Paty, D. Lummerzheim, and S. W. Bougher (2012), On wind-driven electrojets at magnetic cusps in the nightside ionosphere of Mars, *Earth Planets Space*, *64*(2), 93–103, doi:10.5047/eps.2011.04.010.
- Frahm, R. A., et al. (2006a), Carbon dioxide photoelectron energy peaks at Mars, *Space Sci. Rev.*, *126*(1–4), 389–402, doi:10.1007/s11214-006-9119-5.
- Frahm, R. A., et al. (2006b), Locations of atmospheric photoelectron energy peaks within the Mars environment, *Space Sci. Rev.*, *126*(1–4), 389–402, doi:10.1007/s11214-006-9119-5.
- Fränz, M., et al. (2006), Plasma intrusion above Mars crustal fields—Mars Express ASPERA-3 observations, *Icarus*, *182*(2), 406–412, doi:10.1016/j.icarus.2005.11.016.
- Gurnett, D. A., et al. (2005), Radar soundings of the ionosphere of Mars, *Science*, *310*(5756), 1929–1933, doi:10.1126/science.1121868.
- Gurnett, D. A., D. D. Morgan, F. Duru, F. Akalin, J. D. Winningham, R. A. Frahm, E. Dubinin, and S. Barabash (2010), Large density fluctuations in the Martian ionosphere as observed by the Mars Express radar sounder, *Icarus*, *206*(1), 83–94, doi:10.1016/j.icarus.2009.02.019.
- Halekas, J. S., D. A. Brain, R. P. Lin, J. G. Luhmann, and D. L. Mitchell (2008), Distribution and variability of accelerated electrons at Mars, *Adv. Space Res.*, *41*(9), 1347–1352, doi:10.1016/j.asr.2007.01.034.
- Han, X., et al. (2014), Discrepancy between ionopause and photoelectron boundary determined from Mars Express measurements, *Geophys. Res. Lett.*, *41*, 8221–8227, doi:10.1002/2014GL062287.
- Krymskii, A. M., et al. (2002), Structure of the magnetic field fluxes connected with crustal magnetization and topside ionosphere at Mars, *J. Geophys. Res.*, *107*(A9), 1245, doi:10.1029/2001JA000239.
- Lillis, R. J., and D. A. Brain (2013), Nightside electron precipitation at Mars: Geographic variability and dependence on solar wind conditions, *J. Geophys. Res. Space Physics*, *118*, 3546–3556, doi:10.1002/jgra.50171.
- Lillis, R. J., M. O. Fillingim, L. M. Peticolas, D. A. Brain, R. P. Lin, and S. W. Bougher (2009), Nightside ionosphere of Mars: Modeling the effects of crustal magnetic fields and electron pitch angle distributions on electron impact ionization, *J. Geophys. Res.*, *114*, E11009, doi:10.1029/2009JE003379.
- Lundin, R., et al. (2006), Plasma acceleration above Martian magnetic anomalies, *Science*, *311*(5763), 980–983, doi:10.1126/science.1122071.
- Matta, M., M. Mendillo, P. Withers, and D. Morgan (2015), Interpreting Mars ionospheric anomalies over crustal magnetic field regions using a 2-D ionospheric model, *J. Geophys. Res. Space Physics*, *120*, 766–777, doi:10.1002/2014JA020721.
- Mitchell, D. L., R. P. Lin, C. Mazelle, H. Rème, P. A. Cloutier, J. E. P. Connerney, M. H. Acuña, and N. F. Ness (2001), Probing Mars' crustal magnetic field and ionosphere with the MGS electron reflectometer, *J. Geophys. Res.*, *106*(E10), 23,419–23,428, doi:10.1029/2000JE001435.
- Morgan, D. D., D. A. Gurnett, D. L. Kirchner, J. L. Fox, E. Nielsen, and J. J. Plaut (2008), Variation of the Martian ionospheric electron density from Mars Express radar soundings, *J. Geophys. Res.*, *113*, A09303, doi:10.1029/2008JA013313.
- Němec, F., D. D. Morgan, D. A. Gurnett, and F. Duru (2010), Nightside ionosphere of Mars: Radar soundings by the Mars Express spacecraft, *J. Geophys. Res.*, *115*, E12009, doi:10.1029/2010JE003663.
- Němec, F., D. D. Morgan, D. A. Gurnett, and D. A. Brain (2011), Areas of enhanced ionization in the deep nightside ionosphere of Mars, *J. Geophys. Res.*, *116*, E06006, doi:10.1029/2011JE003804.
- Nielsen, E., X.-D. Wang, D. A. Gurnett, D. L. Kirchner, R. Huff, R. Orosei, A. Safaeinili, J. J. Plaut, and G. Picardi (2007a), Vertical sheets of dense plasma in the topside Martian ionosphere, *J. Geophys. Res.*, *112*, E02003, doi:10.1029/2006JE002723.
- Nielsen, E., et al. (2007b), Local plasma processes and enhanced electron densities in the lower ionosphere in magnetic cusp regions on Mars, *Planet. Space Sci.*, *55*(14), 2164–2172, doi:10.1016/j.pss.2007.07.003.
- Picardi, G., et al. (2004), MARSIS: Mars Advanced Radar for Subsurface and Ionospheric Sounding, in *Mars Express: A European Mission to the Red Planet*, edited by A. Wilson, pp. 51–69, ESA Publ. Div., Noordwijk, Netherlands.
- RiOUSset, J. A., C. S. Paty, R. J. Lillis, M. O. Fillingim, S. L. England, P. G. Withers, and J. P. M. Hale (2013), Three-dimensional multifluid modeling of atmospheric electrodynamics in Mars' dynamo region, *J. Geophys. Res. Space Physics*, *118*, 3647–3659, doi:10.1002/jgra.50328.
- RiOUSset, J. A., C. S. Paty, R. J. Lillis, M. O. Fillingim, S. L. England, P. G. Withers, and J. P. M. Hale (2014), Electrodynamics of the Martian dynamo region near magnetic cusps and loops, *Geophys. Res. Lett.*, *41*, 1119–1125, doi:10.1002/2013GL059130.
- Safaeinili, A., W. Kofman, J. Mouginot, Y. Gim, A. Herique, A. B. Ivanov, J. J. Plaut, and G. Picardi (2007), Estimation of the total electron content of the Martian ionosphere using radar sounder surface echoes, *Geophys. Res. Lett.*, *34*, L23204, doi:10.1029/2007GL032154.
- Soobiah, Y. I. J., et al. (2006), Observations of magnetic anomaly signatures in Mars Express ASPERA-3 ELS data, *Icarus*, *182*(2), 396–405, doi:10.1016/j.icarus.2005.10.034.
- Soobiah, Y. I. J., S. Barabash, H. Nilsson, G. Stenberg, R. Lundin, A. J. Coates, J. D. Winningham, and R. A. Frahm (2013), Energy distribution asymmetry of electron precipitation signatures at Mars, *Planet. Space Sci.*, *76*, 10–27, doi:10.1016/j.pss.2012.10.014.
- Withers, P., M. J. Mendillo, H. Rishbeth, D. P. Hinson, and J. Arkan-Hamed (2005), Ionospheric characteristics above Martian crustal magnetic anomalies, *Geophys. Res. Lett.*, *32*, L16204, doi:10.1029/2005GL023483.